Received: 16 February 2021 | Revised: 15 July 2021 | Accepted: 16 July 2021

DOI: 10.1002/nme.6792

RESEARCH ARTICLE

WILEY

A fast Fourier transform based method for computing the effective crack energy of a heterogeneous material on a combinatorially consistent grid

Felix Ernesti | **Matti Schneider**

Institute of Engineering Mechanics, Karlsruhe Institute of Technology (KIT), Karlsruhe, Germany

Correspondence
Matti Schneider, Institute of Engineering Mechanics, Karlsruhe Institute of Technology (KIT), Karlsruhe, Germany.
Email: matti.schneider@kit.edu

Funding information
Deutsche Forschungsgemeinschaft, Grant/Award Numbers: GRK 2078, SCHN 1595/2

Abstract

This work is concerned with computing the effective crack energy of periodic and random media which arises in mathematical homogenization results for the Francfort–Marigo model of brittle fracture. A previous solver based on the fast Fourier transform (FFT) led to solution fields with ringing or checkerboard artifacts and was limited in terms of the achievable accuracy. As computing the effective crack energy may be recast as a continuous maximum flow problem, we suggest using the *combinatorial continuous maximum flow* discretization introduced by Couprie et al. The latter is devoid of artifacts, but lacks an efficient large-scale solution method. We fill this gap and introduce a novel solver which relies upon the FFT and a doubling of the local degrees of freedom which is resolved by the alternating direction method of multipliers (ADMM). Last but not least we provide an adaptive strategy for choosing the ADMM penalty parameter, further speeding up the solution procedure. We demonstrate the salient features of the proposed approach on problems of industrial scale.

KEYWORDS

alternating direction method of multipliers, combinatorial continuous maximum flow, effective crack energy, FFT-based computational homogenization

1 | INTRODUCTION

1.1 | State of the art

Modern fracture mechanics[1] originated from the pioneering work of Griffith,[2] who postulated a criterion for the quasi-static growth of a preexisting crack in a brittle, isotropic and elastic solid based on an energetic reasoning. More precisely, he considered the change of the potential energy Π with the crack area A and postulated that a crack can only grow whenever the energy release rate $-d\Pi/dA$ reaches a critical value γ. Put differently, the crack grows whenever it is energetically more favorable to increase the surface energy of the crack than to increase the elastic energy stored in the body.

For three-dimensional isotropic elasticity and a semi-infinite planar preexisting crack in an infinite medium, Irwin[3] shifted the attention to the $r^{-\frac{1}{2}}$-stress singularity at the crack tip where r denotes the Euclidean distance to the crack

tip. He distinguished three different modes which quantify the degree of singularity of the normal, the in-plane and the out-of-plane shear stresses, respectively, and associated a stress-intensity factor to each mode. Expressing the energy-release rate in terms of these stress-intensity factors, Irwin converted Griffith's criterion into an investigation of the associated stress concentration at the crack tip.[4]

Independently, Cherepanov[5] and Rice[6] proposed a clever way to compute the local energy-release rate at a crack trip in terms of a contour integral around the crack tip, the so-called J-integral. This J-integral offers an elegant way to deal with the stress singularity at the crack tip numerically, as it is independent of the chosen path of integration.

Griffith's criterion presupposes the crack path to be known in advance, that is, it may only be used for assessing *when* a crack propagates, and not for predicting *how* it grows. To predict the latter, the most common approaches exploit the principle of local symmetry[7] or follow the postulate of maximum energy-release.[8]

Linear elastic fracture mechanics was also extended to account for elastoplastic effects, see Dugdale[9] and Barenblatt[10] for early contributions. Classical finite-element methods may be used in computational approaches to fracture mechanics, for instance by computing the stress-intensity factors numerically.[11] However, it turns out to be difficult to resolve the singularity at the crack tip. For this purpose, enriched[12] or extended[13] finite-element discretizations were developed, which account for the crack-tip by adding special ansatz functions to cracked elements.

Driven by the use of anisotropic materials in industrial practice, in particular wood and composites, linear elastic fracture mechanics was extended to (homogeneous) anisotropic brittle solids.[14-16] All three aforementioned pillars, Griffith's energy release rate, Irwin's stress intensity factors and techniques based on the J-integral may be extended to this scenario, and the formulas become particularly simple for self-similar crack growth, see William's review article.[17] Some care has to be taken, as the fracture modes are not directly correlated to the normal and tangential jumps in the crack displacement.[18]

Francfort and Marigo[19] revisited Griffth's original proposition in the quasi-static setting in order to include crack nucleation and crack branching, utilizing a variational formulation. More precisely, for a given body Ω and after a discretization in pseudo-time, they seek the displacement u and the crack surface S as minimizers of the Francfort–Marigo functional

$$FM(u,S) = \frac{1}{2}\int_{\Omega\setminus S} \nabla^s u(x) : \mathbb{C}(x) : \nabla^s u(x)\, dx + \int_S \gamma(x)\, dA \tag{1}$$

under the constraint of crack irreversibility, that is, that the crack set S must contain the crack set of the previous time step. Here, $\nabla^s u$ denotes the symmetrized gradient of the displacement field, that is, the strain tensor field, $\mathbb{C}$ refers to the stiffness tensor and γ denotes the critical energy release rate. Some care has to be taken with the formulation (1), as Griffith's original proposal concerns only critical points of the functional (1) including local minima, local maxima and saddle points, whereas a rigorous mathematical treatment[20] of the Francfort–Marigo model (1) appears to be limited to *global minimizers*. Please note that the formulation (1) accounts for heterogeneities in a natural way.

A pertinent numerical approach to minimize the Francfort–Marigo functional (1) was introduced by Bourdin,[21] developed in close analogy to the Ambrosio–Tortorelli approximation of the Mumford–Shah functional. For each pseudo-time step, a displacement field u and a scalar damage variable d are sought which minimize the phase-field energy functional

$$PF_\eta(u,d) = \frac{1}{2}\int_\Omega (1-d(x))^2 \nabla^s u(x) : \mathbb{C}(x) : \nabla^s u(x) + \gamma(x)\left[\frac{d(x)^2}{4\eta} + \eta\, \|\nabla d(x)\|^2\right] dx, \tag{2}$$

involving a length-scale parameter η. For $\eta \to 0$, the functional (2) Γ-converges to the Francfort–Marigo functional (1). The numerical strategy based on minimizing the functional (2) may be interpreted as a nonlocal damage model[22,23] involving the length-scale parameter η. Due to its similarity to phase-field models, however, this class of numerical approximations is nowadays referred to as phase-field fracture models.[24,25]

Owing to their ability to nucleate cracks and to produce complex crack patterns, phase-field fracture models were subject to a flurry of activity, see Ambati et al.[26] for a review. In particular, strategies to account for material anisotropy in the phase-field framework[27-29] were proposed. As for linear elastic fracture mechanics of anisotropic media, such models may require elaborate and expensive experimental techniques to identify the material parameters.

To alleviate this burden, multiscale methods, in particular homogenization approaches, proved to be very effective for elastic and hardening-type inelastic material behavior. We refer to Matouš et al.[30] for a recent overview. Unfortunately, when leaving the realm of hardening-type material behavior, multiscale methods face difficulties. For example, Gitman et al.[31] considered a nonlocal damage model with softening behavior and showed by numerical simulations that, in the

post-peak loading regime, the average stress response tends to zero as the size of the volume element goes to infinity. In particular, the strategy of computing effective quantities via simulations on representative volume elements—which works well for hardening-type materials—leads to useless results in case of softening.

This difficulties with upscaling softening damage or fracture, in particular for complex materials as shown in Figure 1, become apparent from different perspectives. Classically, a sufficient condition for homogenization to be applicable is a scale separation between the heterogeneities on the microscale and the typical change of the fields of interest on the macroscale. For a crack, however, the stress is singular at the crack tip, and this sufficient condition does not hold. From another perspective, let us consider a nonlocal damage model. The nonlocality is necessary to arrive at mesh-independent results for a corresponding finite-element model. Thus, two scales are present in such a multiscale nonlocal damage model—the typical scale of heterogeneity and the length scale of the nonlocality. In upscaling, the scale of heterogeneity is small, and we wish to pass to the limit of vanishing heterogeneity size. Fixing the nonlocal length scale upon homogenization means that the nonlocality essentially screens the influence of the heterogeneities. Tying the nonlocal length scale to the size of the heterogeneities, however, means that the mesh-dependence of the damage model is recovered upon homogenization, rendering the procedure illegitimate. Of course, computations of nonlocal damage models[34,35] or phase-field fracture[36-38] on microstructures may be pursued. Unfortunately, connecting the results to macroscopic material properties appears challenging as the apparent stresses are inherently size-dependent, see Gitman et al.[31]

More to the point, the actual form of the effective model is at the heart of the problem. Only in the isotropic and linear elastic case, there appears to be a universal agreement on the physics of brittle fracture. In particular, the notions of crack resistance, critical energy-release rate and fracture toughness coincide, and represent a scalar material parameter. Upon generalization, such an agreement of the different notions may be lost. Consider, for instance, a heterogeneous material and a crack propagating under quasi-static loading. When crossing a material boundary, in general, the energy-release rate evaluated on the fly will be a function of time, that is, it may change with each loading increment. Then, it remains to *define* the macroscopic, that is, *effective*, crack resistance, for instance as the maximum or the mean of the encountered values. We do not intend to evaluate these proposals here, but rather stress that there appears to be some disagreement on the notion of "effective crack resistance" in the literature, and care has to be taken when comparing these notions.

In the context of classical linear elastic fracture mechanics, Bower-Ortiz[39] provided a perturbative solution for a semi-infinite crack passing through a single, tough inclusion in a matrix. Roux et al.[40] discussed an emerging effective crack resistance for a material whose elastic properties are isotropic and homogeneous, and only the crack resistance is heterogeneous. In this context, a self-consistent method for estimating the effective fracture toughness of a planar crack propagating through inclusions is established. For a medium with randomly distributed heterogeneities, they identified

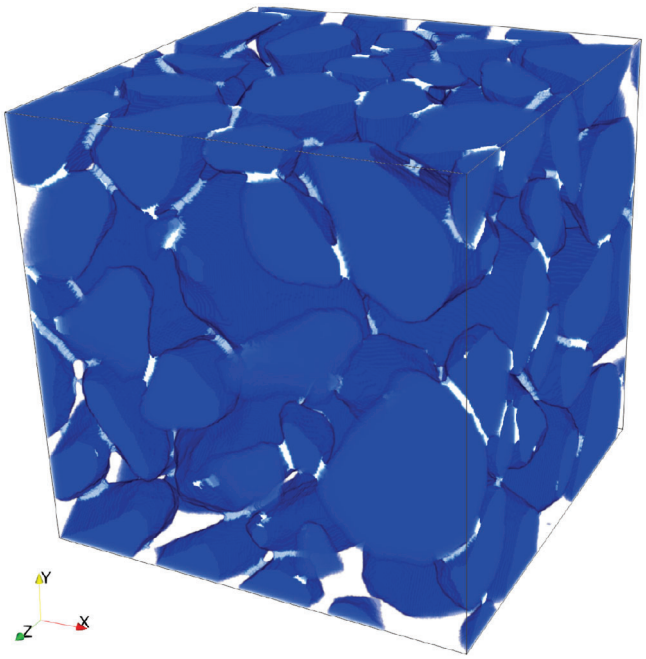

FIGURE 1 Complex microstructure of bound sand[32,33]

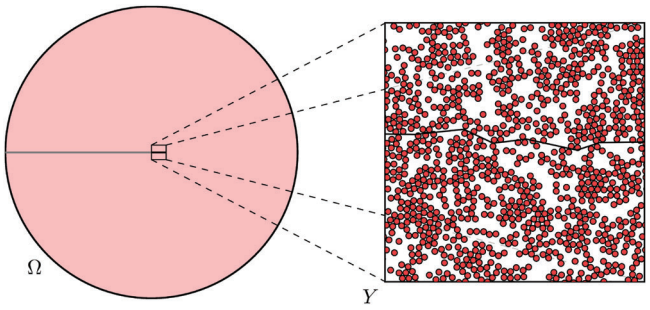

FIGURE 2 Schematic of a crack increment in a microstructured material

regions of weak pinning, where the fracture toughness is given by the arithmetic mean of the local toughness, and strong pinning, where a much higher toughness emerges, see also Démery et al.[41] for a related study. Lebihain and coworkers[42,43] extended the mentioned studies by accounting for cracks which bypass an inclusion, based on a perturbative, coplanar approach.[44]

To account for a heterogeneity in the elastic properties, Hossain et al.[45] performed phase-field fracture computations on heterogeneous microstructures with specific, so-called "surfing" boundary conditions. The emerging effective crack resistance equals the maximum in time of the J-integral evaluated along the crack tip, see also Kuhn-Müller[46] and Brach et al.[47]

As an alternative to these approaches, Braides et al.[48] proved a mathematical homogenization result for the Mumford–Shah functional, which corresponds to the Francfort–Marigo[19] model upon antiplane-shear loading. More precisely, in a quasi-static setting and after a discretization in pseudo-time, Braides et al.[48] consider a fixed periodic microstructure (with nondegenerate stiffness and crack resistance), and identify the Γ-limit for vanishing period as the functional

$$FM_{\text{eff}}(u,S) = \frac{1}{2}\int_{\Omega\setminus S} \nabla^s u(x) : \mathbb{C}_{\text{eff}} : \nabla^s u(x)\, dx + \int_S \gamma_{\text{eff}}\left(\bar{\xi}\right)\, dA, \tag{3}$$

where $\bar{\xi}$ denotes the unit normal to the crack surface S. Here, the (possibly anisotropic) effective stiffness tensor $\mathbb{C}_{\text{eff}}$ arises from the usual elastic homogenization formula based on the classical cell problem.[49] The integrand γ_{eff} of the surface term is a function of a unit vector, and may be computed by a corrector problem involving the local crack resistances only. However, in contrast to the elastic contribution, the latter surface term involves an infinite-volume limit, as standard for stochastic homogenization,[50-52] also for periodic materials. For cells of finite size, the surface term $\gamma_{\text{eff}}(\bar{\xi})$ may be interpreted as finding the γ-weighted minimal surface with average normal $\bar{\xi}$ cutting the microstructure.[53]

In particular, the volumetric and the surface energies decouple upon homogenization, as a result of the different scalings of these terms in the model (1). Subsequently, the homogenization statement was extended to the case of stationary and ergodic random materials,[54] that is, in engineering terms, the existence of representative volume elements,[55,56] separately for the bulk and the surface part, is ensured. Please note that this volume-surface decoupling is a consequence of the assumed nondegeneracy of the integrands. In case of degeneracy, an interaction of the two terms is not excluded, see Barchiesi et al.[57] and Pellet et al.[58]

Recently, Friedrich[59] showed the homogenization result (3) for linear elasticity (without the restriction to anti-plane shear). Let us also highlight that the effective model (3) also emerges when homogenizing the Ambrosio–Tortorelli approximation of the Francfort–Marigo model, that is, phase-field fracture models, see Bach et al.[60]

Let us put the homogenization result (3) into context. The heterogeneous fracture problem involves two prominent length scales: the correlation length of the heterogeneities and the typical size of a displacement increment. Classically, owing to the quasi-static framework, the size of the displacement increment is assumed infinitesimal. In this interpretation, a crack propagates through a microstructure, and its progress may be hindered by various factors, like being pinned to an interface. This interpretation is implicit in Hossain et al.,[45] for example. In practical applications, however, the displacement increment is typically of the order of the macroscopic scale. By contrast, Braides et al.[48] fix the displacement increment once and for all, and pass to the limit of infinitesimally small heterogeneities, see Figure 2 for an illustration.

Another difference is the understanding of the emerging *effective* properties. As Hossain et al.[45] always consider a time-continuous problem, their crack resistance is defined as the maximum in time of the local J-integral. By contrast, Braides et al.[48] practically work with an energy equivalence between the macroscopic fracture energy and the microscopic fracture energy, as a result of their energetic framework.

Last but not least, let us remark that Γ-convergence implies the convergence of *absolute* minimizers, but does not predict what happens to *local* minimizers. Although an energy equivalence between the microscopic fracture energy and the macroscopic fracture energy appears in a natural way, the (absolutely) minimal surface in the cell problem appears to be a byproduct of Γ-convergence. From a physical point of view, it might be more appropriate to work with crack surfaces that are just local minima of the weighted area. Still, with assessing the safety of microstructured components in mind, the absolutely minimal surface serves as a lower bound for the (real) effective crack energy, and is furthermore robust w.r.t. stochastic fluctuations in the microstructure. To stress the difference to the crack resistance, we will reserve the terminology "effective crack energy" for the surface integrand γ_{eff}.

Minimizing the fracture energy has been considered earlier by Jeulin[61] for predicting crack propagation on two-dimensional micrographs. In fact, in two spatial dimension, the problem of computing the effective crack energy simplifies drastically. Indeed, it reduces to the problem of computing minimum (weighted) geodesics, for which efficient algorithms are available.[62,63]

A method for computing the effective crack energy for three-dimensional solids based on the homogenization result of Braides[48] and following contributions was proposed by Schneider.[53] The approach is based on a convex reformulation of the minimum-cut problem[64] in terms of maximum flow. More precisely, a primal-dual hybrid gradient method[65,66] was used, extending previous FFT-based computational homogenization methods for thermal conductivity and elasticity.

1.2 | Contributions

This work is concerned with computing the effective crack energy via an appropriate cell formula (to be discussed in Section 2.1) corresponding to the mathematical homogenization results.[48,54,59] Please note that the computed effective crack energy may differ from the *effective crack resistance*, depending on the underlying length scales and loading scenarios (see section 2.1, item 5, in Schneider[53] for a discussion). Still, the computed effective crack energy gives rise to a lower bound for the effective crack resistance, and may thus be used for assessing the safety of components made of such composites.

Previous work[53] provided a computational approach for computing the effective crack energy using an FFT-based primal-dual hybrid gradient solver and two discretization schemes, that is, trigonometric collocation and the rotated staggered grid. The approach[53] has two shortcomings. First, the solution fields are characterized by ringing or checkerboard artifacts, depending on the discretization. Moreover, the solver does not permit reaching a high accuracy for complex three-dimensional microstructures. Although the first shortcoming concerns the discretization and the second issue is related to the numerical resolution, both effects are actually related. Indeed, as computing the effective crack energy involves a pointwise constraint on a vector field, discretization-related artifacts may interfere with solver performance.

The cell problem for computing the effective crack energy is closely related to the minimum-cut problem put forward by Strang[64] in his analysis of the continuous maximum flow problem, see Section 2.1. To be more precise, the maximum flow problem is rooted in graph theory and seeks a feasible flow through a flow network that obtains the maximum possible flow rate under capacity constraints.[67] With the help of duality theory for linear programming, it may be shown that the maximum flow equals the minimum capacity of a cut disconnecting the source and the sink.[67,68] Strang[64] proposed a continuum generalization of the graph-theoretic maximum flow problem, involving an incompressible flow field subject to a (continuous) capacity constraint. Similar to the graph-theoretic version, he established a duality result which equates the maximum flow rate with the capacity of a minimum cut. However, the continuous version is no longer based on *linear* duality theory, and requires more sophisticated mathematical tools. Previous work[53] realized that the cell problem corresponding to the mathematical homogenization results[48,54,59] may be interpreted as a minimum-cut problem, where the microscopic (heterogeneous) crack resistance is regarded as a (spatially varying) capacity. Then, the maximum flow-minimum cut duality, valid on a discrete level, is invoked to construct a suitable primal-dual solver.

For the graph-theoretic maximum flow problem, a variety of efficient solvers is available.[67,69-71] Unfortunately, these solvers are unsuited for the continuous maximum flow problem. Indeed, working with a graph-theoretic discretization leads to so-called metrication artifacts, which do not vanish upon mesh refinement.[72] More precisely, for the graph-theoretic version, the capacity constraints are associated to the edges, whereas, when representing the continuous

maximum flow problem in terms of a finite difference discretization, the capacity constraints are associated to the nodes of the graph. As a remedy, Couprie et al.[73] introduced the *combinatorial continuous maximum flow* (CCMF) discretization, whose node-based capacity constraints account for all adjacent edges in a suitable way. The CCMF discretization, to be discussed in Section 2.2, naturally avoids metrication errors, and may be implemented into standard convex optimization solvers.[74] However, as the authors remark themselves: "In 3D, our CCMF implementation is suffering from memory limitations in the direct solver we used, limiting its performances" [73, sec. 4.4.3].

Our contributions are threefold. For a start, we propose using the CCMF discretization for the effective crack energy associated to the mathematical homogenization results,[48,54,59] see Section 2 for details. In this way, the artifacts of the previously used discretizations[53] are fully eliminated. Our second contribution concerns a novel FFT-based solver for the maximum flow problem in the CCMF discretization on regular periodic grids, filling the gap mentioned by Couprie et al.[73] The proposed solver, see Section 3, is based on a doubling of the degrees of freedom per cell, which makes the nonlocal capacity constraint for the CCMF discretization *local*, at the expense of additional constraints enforcing compatibility of the flow field across the faces of the voxel grid. As a byproduct, we arrive at an expression for the minimum-cut problem that is much simpler than in Couprie et al.,[73] see Section 3.1. Then, the alternating direction method of multipliers (ADMM), pioneered by Michel et al.[75,76] in conjunction with FFT-based methods, is used to extract the minimum cut, see Section 3.2. Last but not least, we study recently proposed,[77] adaptive strategies for choosing the penalty parameter in the ADMM. Finally, we demonstrate the capabilities of our approach in applications of industrial size, see Section 4. We find that an adaptive parameter-selection strategy is critical for high performance and high accuracy, improving upon the standard ADMM used by Willot,[78] who treats the closely related graph-based maximum flow problem (not the continuous one).

2 | THE EFFECTIVE CRACK ENERGY OF A HETEROGENEOUS MATERIAL

2.1 | Cell formulae for the minimum cut and the maximum flow

Let us consider a cuboid cell $Y = [0, L_1] \times [0, L_2] \times [0, L_3]$, on which a heterogeneous field of crack resistances* $\gamma : Y \to \mathbb{R}$ is given. For mathematical reasons, we suppose that there are positive constants $\gamma_\pm$, s.t. the inequalities

$$\gamma_- \leq \gamma(x) \leq \gamma_+ \quad \text{hold for all} \quad x \in Y.$$

We define the effective crack energy γ_{eff},[48,53,54] a function on the unit sphere $S^2 \subseteq \mathbb{R}^3$, by

$$\gamma_{\text{eff}}(\bar{\xi}) = \inf_{\phi} \frac{1}{|Y|} \int_Y \gamma \left\| \bar{\xi} + \nabla \phi \right\| dx, \quad \bar{\xi} \in S^2, \tag{4}$$

see Figure 3, where $|Y| = L_1 L_2 L_3$ denotes the volume of the cell and the infimum is evaluated over all smooth scalar fields $\phi : Y \to \mathbb{R}$ which are periodic, together with all their derivatives. This formula computes the (periodic) minimum cut through the cell Y with mean normal $\bar{\xi}$ as a γ-weighted minimal surface. The scalar ϕ plays the role of a characteristic function jumping across the cut. Please note that the integrand in the right-hand side of Equation (4) is a function which is homogeneous of degree one, that is, it satisfies $f(\lambda\xi) = \lambda f(\xi)$ for all vectors $\xi \in \mathbb{R}^3$ and all scalars $\lambda > 0$. This contrasts with thermal conductivity,[49] where a homogeneity of degree two leads to a linear Euler–Lagrange equation associated to the variational problem.

For the problem at hand (4), additional complications arise. For a start, due to the one-homogeneity, the functional in the definition (4) is not differentiable. In particular, the first-order necessary conditions are (strongly) nonlinear. Furthermore, the one-homogeneity permits *localization* to appear for minimizers of the variational problem (4). This localization is not unwarranted, as such minimizers actually represent minimum cuts through the microstructure,[64] weighted by the crack resistance, and enable computing the effective crack energy by the local crack resistance averaged over the

*For homogeneous, isotropic materials under certain loading conditions, the term crack resistance, also known as critical energy-release rate, may be used interchangeably with the notion of fracture toughness, as Griffith's[2] energetic criterion may be equivalently rewritten in terms of stress-intensity factors,[3] see Gross and Seelig [1, ch. 4.6]. In the heterogeneous case, however, this is may not be the case. We therefore restrict to the term crack resistance, avoiding the term fracture toughness altogether.

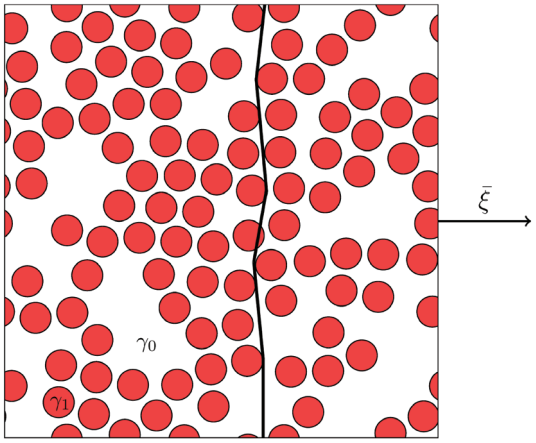

FIGURE 3 Schematic of a potentially minimal crack traversing a two-phase microstructure for prescribed normal $\bar{\xi}$

minimum cut. In fact, the minimum cut need not be unique. However, the computed effective crack energy is unique as a consequence of the convexity of the functional to be minimized.

To circumvent the inherent lack of differentiability characterizing the functional (4), dual and primal-dual formulations may be exploited.[79] As an example, the (formal) dual to the variational problem is given by the maximum flow problem[64]

$$\frac{1}{|Y|}\int_Y v\cdot\bar{\xi}\,dx \to \max_{\substack{\operatorname{div} v=0\\ \|v\|\leq\gamma}}, \tag{5}$$

where the maximum is evaluated over all smooth and solenoidal vector fields $v : Y \to \mathbb{R}^3$ which satisfy the pointwise constraint

$$\|v(x)\| \leq \gamma(x) \quad \text{for (almost) all} \quad x \in Y. \tag{6}$$

Due to the nonnegativity of the terms involved, the latter condition may also be recast in the form

$$\|v(x)\|^2 \leq \gamma(x)^2 \quad \text{for (almost) all} \quad x \in Y. \tag{7}$$

The dual problem (5) maximizes the total flow in direction $\bar{\xi}$ through the microstructure under the pointwise constraints (6). The advantage of the dual formulation (5) over the primal formulation (4) is that it represents a smooth (in fact linear) optimization problem with linear and quadratic constraints, for which powerful solution methods are available.[74] However, some caution is advised, as the primal (4) and the dual problem (5) are strongly dual in the continuous setting only for a *continuous* crack resistance γ.[64] As soon as the crack resistance γ is discontinuous, explicit counterexamples[80] to strong duality are known, that is, the maximum computed in the dual problem (5) is strictly less than the minimum computed for the primal problem (4).

For practical considerations, this delicacy does not play much of a role. Indeed, in finite dimensions, convex optimization problems with convex constraints *always* satisfy strong duality provided Slater's condition is satisfied [74, sec. 5.2]. Slater's condition states that there is a strictly feasible point, that is, a point where all inequality constraints are satisfied as strict inequalities. Due to our prerequisite $\gamma \geq \gamma_- > 0$, the field $v \equiv 0$ is strictly feasible for the dual problem (5), and strong duality holds upon discretization. In particular, we may exploit the maximum flow formulation (5), as long as it arises by formal Lagrangian dualization [74, ch. 5] of a discretization of the cell problem (4).

2.2 | The combinatorial continuous maximum flow discretization

In this section, we discuss the combinatorial continuous maximum flow discretization (CCMF)[73] for the special case of regular grids and in the periodic setting. The discretization scheme naturally approximates the continuous maximum flow formulation (5), and we take it as our point of departure.

For this purpose, suppose that the unit cell $Y = [0, L_1] \times [0, L_2] \times [0, L_3]$ is discretized by a regular grid with N_i $(i = 1, 2, 3)$ voxels for each coordinate direction. Each voxel is assumed to be cubic with edge length h, that is, the conditions $h = L_i/N_i$ $(i = 1, 2, 3)$ are assumed to hold. In a finite volume discretization, where each individual voxel serves as a control volume, the flow between adjacent cells is quantified by a flow field v, which is located at the voxel faces, see Figure 4. The conservation of mass is encoded by the balance of in- and outflow

$$0 = v\left[i+\frac{1}{2},j,k\right] - v\left[i-\frac{1}{2},j,k\right] + v\left[i,j+\frac{1}{2},k\right] - v\left[i,j-\frac{1}{2},k\right] + v\left[i,j,k+\frac{1}{2}\right] - v\left[i,j,k-\frac{1}{2}\right], \tag{8}$$

where we tacitly assume the integer indices i, j, k to satisfy

$$0 \le i < N_1, \quad 0 \le j < N_2 \quad \text{and} \quad 0 \le k < N_3,$$

and the Equation (8) should be interpreted in a periodic fashion. Let us denote by

$$\gamma[i,j,k] = \gamma\left(\left(i+\frac{1}{2}\right)h, \left(j+\frac{1}{2}\right)h, \left(k+\frac{1}{2}\right)h\right)$$

the evaluations of the crack resistance γ at the voxel centers, which we sample on a discrete grid Y_N. Then, for the CCMF-discretization, the constraint (6) is approximated by the $N_1N_2N_3$ constraints

$$v\left[i+\frac{1}{2},j,k\right]^2 + v\left[i-\frac{1}{2},j,k\right]^2 + v\left[i,j+\frac{1}{2},k\right]^2 + v\left[i,j-\frac{1}{2},k\right]^2 + v\left[i,j,k+\frac{1}{2}\right]^2 + v\left[i,j,k-\frac{1}{2}\right]^2 \le 2\,\gamma[i,j,k]^2. \tag{9}$$

Here, the constraint (9) is associated to each cell, and accounts for all six in- and outflow variables located on the corresponding adjacent faces, see Figure 4. Compared with the continuous formulation (7), which involves a vector of dimension three, twice the number of terms is considered. This is compensated by adding a factor two on the right-hand side.

Then, for prescribed average crack normal $\overline{\xi} \in S^2$, the CCMF discretization approximates the maximum flow problem (5) by the maximization problem

$$\frac{1}{N_1N_2N_3}\sum_{i,j,k} \overline{\xi}_x\, v\left[i+\frac{1}{2},j,k\right] + \overline{\xi}_y\, v\left[i,j+\frac{1}{2},k\right] + \overline{\xi}_z\, v\left[i,j,k+\frac{1}{2}\right] \to \max_{v \text{ satisfying (2.5) and (2.6)}}. \tag{10}$$

With FFT-based solution methods, to be discussed in Section 3, in mind, we transform the natural finite volume formulation into a more compact representation that is simpler to manipulate algebraically. For this purpose, we regard the flow field v as a vector field located at the voxel centers, with the identification

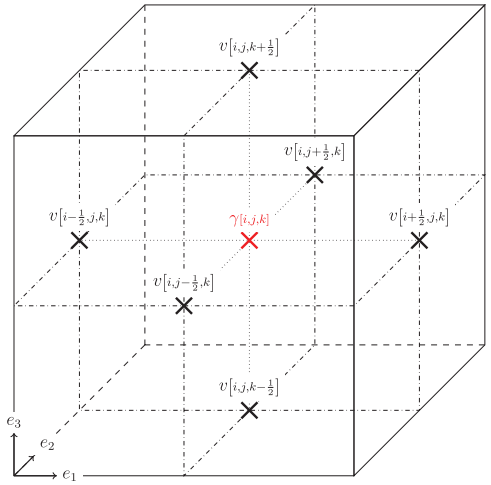

FIGURE 4 Consistent placement of the flow-field variables on a generic voxel cell

$$v_x[i,j,k] = v\left[i+\frac{1}{2},j,k\right],$$

$$v_y[i,j,k] = v\left[i,j+\frac{1}{2},k\right],$$

$$v_z[i,j,k] = v\left[i,j,k+\frac{1}{2}\right].$$

We also introduce a (backwards) divergence-type operator div^- via

$$(\mathrm{div}^- v)\,[i,j,k] = v_x[i,j,k] - v_x[i-1,j,k] + v_y[i,j,k] - v_y[i,j-1,k] + v_z[i,j,k] - v_z[i,j,k-1].$$

Then, the mass conservation (8) is satisfied precisely if $\mathrm{div}^- v = 0$ holds. To encode the constraint (9), we introduce the backwards shift operator S, which operates as follows

$$S(v)[i,j,k] = \begin{bmatrix} v_x[i-1,j,k] \\ v_y[i,j-1,k] \\ v_z[i,j,k-1] \end{bmatrix}. \tag{11}$$

Then, the constraint (9) is equivalent to the condition

$$\|v[i,j,k]\|^2 + \|S(v)[i,j,k]\|^2 \leq 2\,\gamma[i,j,k]^2, \tag{12}$$

expressed in terms of the Euclidean norm of the involved vectors. Last but not least, let us introduce the L^2 inner product on such vector fields

$$\langle v, \tilde{v}\rangle_{L^2} = \frac{1}{N_1 N_2 N_3} \sum_{i,j,k} \left(v_x[i,j,k]\tilde{v}_x[i,j,k] + v_y[i,j,k]\tilde{v}_y[i,j,k] + v_z[i,j,k]\tilde{v}_z[i,j,k] \right) \tag{13}$$

with corresponding norm $\|\cdot\|_{L^2}$. With this notation at hand, we may express the maximization problem (14) in the compact form

$$\langle \bar{\xi}, v\rangle_{L^2} \to \max_{\substack{\mathrm{div}^- v = 0 \\ \|v\|^2 + \|Sv\|^2 \leq 2\gamma^2}}, \tag{14}$$

where we regard $\bar{\xi}$ as a constant vector field and the norm constraint is enforced at every voxel. In the latter formulation, the similarities (and differences) to the continuous formulation (5) become apparent. Indeed, both the objective function and the divergence constraint are discretized in the natural way. The norm constraint, however, is replaced by a "nonlocal" constraint which involves neighboring values of the flow field, as well. Please note that this is a feature rather than a bug, as the flow-field variables are naturally located on the voxel faces, whereas the crack resistance is associated to the voxel center. Instead of *interpolating* the flow-field variables, the CCMF discretization averages the squares of the flow fields. Such an approach has its merits, as will become clear in Section 4.

3 | AN FFT-BASED SOLVER FOR THE CCMF DISCRETIZATION

3.1 | The primal formulation for the CCMF discretization

On a voxel grid, we consider the maximum flow problem (14)

$$\langle \bar{\xi}, v\rangle_{L^2} \to \max_{\substack{\mathrm{div}^- v = 0 \\ \|v\|^2 + \|Sv\|^2 \leq 2\gamma^2}} \tag{15}$$

in the combinatorial continuous maximum flow (CCMF) discretization. With FFT-based resolution in mind, we compute the corresponding Lagrangian dual, that is, the associated minimum cut problem.

For later reference please notice that the adjoint of the backward shift operator S (11) w.r.t. the inner product (13) is given by the (periodized) *forward* shift operator

$$S^*(v)[i,j,k] = \begin{bmatrix} v_x[i+1,j,k] \\ v_y[i,j+1,k] \\ v_z[i,j,k+1] \end{bmatrix}. \tag{16}$$

In particular, as backward and forward shifting are mutual inverses, the equation $S^*S = \mathrm{Id}$ holds in terms of the identity operator Id.

The shift operator is nonlocal, which makes the inequality constraint in the maximum flow problem (15) nonlocal, as well. With computational resolution in mind, we seek a local formulation that relies upon a doubling of dimension. For this purpose, we introduce the linear extension operator A, acting on vector fields v via

$$(Av) = \frac{1}{\sqrt{2}} \begin{bmatrix} v \\ Sv \end{bmatrix}, \tag{17}$$

and producing a vector field with six scalar components per voxel. Then, the problem (15) may be expressed in the equivalent form

$$\langle \bar{\xi}, v \rangle_{L^2} \to \max_{\substack{\mathrm{div}^- v = 0 \\ \|Av\| \leq \gamma}}, \tag{18}$$

where the factor two in front of the crack resistance (15) was transferred into the A-operator (17) and the norm in the constraint refers to the Euclidean norm of vectors with six components. For later reference, let us remark that the adjoint of the operator A (17) w.r.t. the six-component version of the L^2 inner product (13) is given by

$$A^* \begin{bmatrix} w_1 \\ w_2 \end{bmatrix} = \frac{1}{\sqrt{2}}(w_1 + S^* w_2) \tag{19}$$

in terms of the backward shift operator (16). In particular, it holds

$$A^*Av = \frac{1}{2}(v + S^*Sv) = v,$$

that is, $A^*A = \mathrm{Id}$ and $\|A\| = 1$ in operator norm. Thus, the operator A is an isometric embedding, and the operator A^* is a left inverse to the operator A. In turn, the operator AA^* is the orthogonal projector onto the image of the operator A. To complete the necessary notation, we define the indicator function ι_T of a set T via

$$\iota_T(u) = \begin{cases} 0 & u \in T \\ +\infty, & \text{otherwise,} \end{cases}$$

which permits encoding a constraint to the set T in terms of an objective function.

With the necessary terminology at hand, we turn our attention to deriving the Lagrangian dual of the maximum flow problem (15) in the constrained form

$$\langle \bar{\xi}, v \rangle_{L^2} - \iota_{\{\mathrm{div}^- v = 0\}}(v) - \iota_{C_\gamma}(w) \to \max_{w + Av = 0}, \tag{20}$$

where we denote by C_γ the set

$$C_\gamma = \left\{ w : Y_N \to \mathbb{R}^6 \;\middle|\; \|w[i,j,k]\| \leq \gamma[i,j,k] \quad \text{for all} \quad i,j,k \right\}. \tag{21}$$

The associated Lagrangian function reads

$$L(v,w,\xi) = \langle \bar{\xi}, v\rangle_{L^2} - \iota_{\{\mathrm{div}^- v=0\}}(v) - \iota_{\mathcal{C}_\gamma}(w) - \langle \xi, Av + w\rangle_{L^2} \tag{22}$$

in terms of the Lagrangian multiplier field $\xi : Y_N \to \mathbb{R}^6$. To evaluate the dual function

$$\varphi(\xi) = \sup_{v,w} L(v,w,\xi),$$

we rearrange the expression of the Lagrangian (22)

$$\begin{aligned}\varphi(\xi) &= \sup_v \langle \bar{\xi}, v\rangle_{L^2} - \iota_{\{\mathrm{div}^- v=0\}}(v) - \underbrace{\langle \xi, Av\rangle_{L^2}}_{=\langle A^*\xi, v\rangle_{L^2}} + \sup_w \langle \xi, w\rangle_{L^2} - \iota_{\mathcal{C}_\gamma}(w) \\ &= \begin{cases} \frac{1}{N_1N_2N_3}\sum_{i,j,k}\gamma[i,j,k]\ \|\xi[i,j,k]\|, & \xi \in \mathcal{K}_{\bar{\xi}}, \\ +\infty, & \text{otherwise}, \end{cases}\end{aligned}$$

in terms the set of compatible normal fields

$$\mathcal{K}_{\bar{\xi}} = \left\{ \xi : Y_N \to \mathbb{R}^6 \;\middle|\; \text{there is some} \quad \phi : Y_N \to \mathbb{R},\ \text{s.t.} \quad A^*\xi = \bar{\xi} + \nabla^+\phi \right\}. \tag{23}$$

This set may be interpreted as follows. Fields $\xi : Y_N \to \mathbb{R}^6$ associate to every voxel six scalar values. These values are assigned to each face of the voxel. Please note that any face of the voxel mesh is thus assigned with *two* values, one for each adjacent voxel. Up to a factor $\sqrt{2}$, $A^*\xi$ refers to the facewise average of these two values. The set $\mathcal{K}_{\bar{\xi}}$ contains all fields, whose averages $A^*\xi$ are compatible in the sense that they arise as the sum of a constant vector (which is fixed beforehand) and the gradient of a scalar field (one scalar per voxel). Thus, up to the facewise averaging, the compatibility constraint is similar to thermal conductivity or elasticity. The final form

$$\frac{1}{N_1N_2N_3}\sum_{i,j,k}\gamma[i,j,k]\ \|\xi[i,j,k]\| \to \min_{\xi\in\mathcal{K}_{\bar{\xi}}} \tag{24}$$

of the dual to the CCMF problem (15) is remarkably close to the original minimum cut formulation (4), cf. the more involved formulas in Couprie et al. [73, sec. 2.3].

3.2 | An FFT-based ADMM solver

To proceed, we rewrite the optimization problem (24) as an equivalent convex program that is amenable to operator-splitting approaches

$$f(\xi) + g(\xi) \to \min_{\xi} \tag{25}$$

in terms of the convex functions

$$f(\xi) = \iota_{\mathcal{K}_{\bar{\xi}}}(\xi) \quad \text{and} \quad g(\xi) = \frac{1}{N_1N_2N_3}\sum_{i,j,k}\gamma[i,j,k]\ \|\xi[i,j,k]\|.$$

The starting point of operator-splitting approaches is the rewriting of the unconstrained problem (25) in constrained form

$$f(\xi) + g(e) \to \min_{\xi=e}. \tag{26}$$

For solving the problem (26), we utilize the alternating direction method of multipliers (ADMM),[81,82] which was pioneered in the context of FFT-based methods by Michel et al.,[75,76] and applied to nonsmooth optimization by Willot.[78]

For this purpose, we investigate the augmented Lagrangian function

$$L_\rho(\xi, e, v) = f(\xi) + g(e) + \langle v, \xi - e\rangle_{L^2} + \frac{\rho}{2}\|\xi - e\|_{L^2}^2, \tag{27}$$

involving a penalization factor $\rho > 0$ and the Lagrange multiplier $v : Y_N \to \mathbb{R}^6$. The ADMM is based on the three-term recursion

$$\begin{aligned} \xi^{k+1} &= \operatorname{argmin}_\xi L_\rho(\xi, e^k, v^k), \\ e^{k+1} &= \operatorname{argmin}_e L_\rho(\xi^{k+1}, e, v^k), \\ v^{k+1} &= v^k + \rho\,(\xi^{k+1} - e^{k+1}). \end{aligned} \tag{28}$$

Let us investigate the first line more explicitly,

$$\begin{aligned} \xi^{k+1} &= \operatorname{argmin}_\xi L_\rho(\xi, e^k, v^k) \\ &= \operatorname{argmin}_\xi f(\xi) + \langle v^k, \xi\rangle_{L^2} + \frac{\rho}{2}\left\|\xi - e^k\right\|_{L^2}^2 \\ &= \operatorname{argmin}_{\xi\in\mathcal{K}_{\bar\xi}}\left\|\xi - e^k + \frac{1}{\rho}\,v^k\right\|_{L^2}^2. \end{aligned}$$

Thus, ξ^{k+1} arises as the orthogonal projection of the point $e^k - v^k/\rho$ onto the set $\mathcal{K}_{\bar\xi}$,

$$\xi^{k+1} = \mathcal{P}_{\mathcal{K}_{\bar\xi}}\left(e^k - \frac{1}{\rho}\,v^k\right).$$

Let us write down an explicit expression for the projection operator $\mathcal{P}_{\mathcal{K}_{\bar\xi}}$. For given $w : Y_N \to \mathbb{R}^6$, we seek $\xi : Y_N \to \mathbb{R}^6$, s.t.

$$\xi = \mathcal{P}_{\mathcal{K}_{\bar\xi}}(w), \quad \text{i.e.,} \quad \xi = \operatorname{argmin}_{\xi\in\mathcal{K}_{\bar\xi}}\|\xi - w\|_{L^2}^2 \quad \text{holds.} \tag{29}$$

With the help of the orthogonal projector $P = AA^*$ and its orthogonal, complementary projector $Q = \mathrm{Id} - AA^*$, we may decompose the vector field ξ

$$\xi = \xi_P + \xi_Q \quad \text{with} \quad \xi_P = P\xi \quad \text{and} \quad \xi_Q = Q\xi, \tag{30}$$

s.t., by orthogonality,

$$\|\xi\|_{L^2}^2 = \|\xi_P\|_{L^2}^2 + \|\xi_Q\|_{L^2}^2 \tag{31}$$

holds. Then, we may express the set $\mathcal{K}_{\bar\xi}$ in the form

$$\mathcal{K}_{\bar\xi} = \left\{\xi : Y_N \to \mathbb{R}^6 \;\middle|\; \text{there are } \phi : Y_N \to \mathbb{R} \text{ and } \eta : Y_N \to \mathbb{R}^6, \text{s.t. } \xi = A(\bar\xi + \nabla^+\phi) + Q\eta\right\}. \tag{32}$$

To show equivalence of definitions, let us take an element $\xi \in \mathcal{K}_{\bar\xi}$ according to the former definition (23), which was characterized by the defining constraint

$$A^*\xi = \bar\xi + \nabla^+\phi.$$

Then, by definition of ξ_P, we observe

$$\xi_P \equiv P\xi = AA^*\xi = A(\bar\xi + \nabla^+\phi),$$

and ξ is contained in the set (32). Conversely, applying A^* to an element ξ of the set (32) yields

$$A^*\xi = \underbrace{A^*A}_{=\mathrm{Id}}(\bar\xi + \nabla^+\phi) + \underbrace{A^*Q}_{=0}\,\eta = \bar\xi + \nabla^+\phi,$$

which shows that ξ lies in the original set (23). Returning to the projection problem (29)

$$\xi = \operatorname{argmin}_{\xi \in \mathcal{K}_{\bar{\xi}}} \|\xi - w\|_{L^2}^2,$$

we decompose $w = w_P + w_Q$ in the same form (30). Due to the Pythagorean theorem (31), we observe

$$\begin{aligned}\xi &= \operatorname{argmin}_{\xi \in \mathcal{K}_{\bar{\xi}}} \|\xi - w\|_{L^2}^2 \\ &= \operatorname{argmin}_{\xi \in \mathcal{K}_{\bar{\xi}}} \|\xi_P - w_P\|_{L^2}^2 + \|\xi_Q - w_Q\|_{L^2}^2 \\ &= \operatorname{argmin}_{\phi,\eta} \|A(\bar{\xi} + \nabla^+\phi) - w_P\|_{L^2}^2 + \|Q\eta - w_Q\|_{L^2}^2,\end{aligned}$$

where we inserted the definition (32) in the last line. We observe that the optimization problems for the variables ϕ and η *decouple*. The problem for $Q\eta$ is particularly simple, and is solved by $Q\eta = w_Q \equiv Qw$. Using that A is an isometric embedding, the problem for ϕ becomes

$$\left\| \bar{\xi} + \nabla^+\phi - A^* w \right\|_{L^2}^2 \to \min_{\phi}.$$

The corresponding critical point satisfies

$$\operatorname{div}^- \left[\bar{\xi} + \nabla^+\phi - A^* w \right] = 0 \quad \Leftrightarrow \quad \operatorname{div}^-\nabla^+\phi = \operatorname{div}^- A^* w.$$

The latter equation may be solved formally to give

$$\phi = (\operatorname{div}^-\nabla^+)^\dagger \operatorname{div}^- A^* w,$$

where $\dagger$ denotes the Moore–Penrose pseudo inverse. Reinserting the found expressions into the definition (32), we find

$$\xi = A\bar{\xi} + A\nabla^+(\operatorname{div}^-\nabla^+)^\dagger \operatorname{div}^- A^* w + (\mathrm{Id} - AA^*)w,$$

which we may also write in the more convenient form

$$\mathcal{P}_{\mathcal{K}_{\bar{\xi}}}(w) = A\bar{\xi} + (\mathrm{Id} - AA^* + A\Gamma A^*)\, w \quad \text{with} \quad \Gamma = \nabla^+(\operatorname{div}^-\nabla^+)^\dagger \operatorname{div}^-. \tag{33}$$

The second line (28) can be rewritten using Moreau's identity [79, eq. (3.8)] in the form

$$e^{k+1} = \left[v^k + \rho\, \xi^{k+1} - \mathcal{P}_{C_\gamma}\left(v^k + \rho\, \xi^{k+1} \right) \right] / \rho,$$

where $\mathcal{P}_{C_\gamma}$ is the orthogonal projector

$$\left(\mathcal{P}_{C_\gamma}(w)\right)[i,j,k] = \begin{cases} \gamma[i,j,k]\; w[i,j,k] / \|w[i,j,k]\|, & \|w[i,j,k]\| > \gamma[i,j,k], \\ w[i,j,k], & \text{otherwise}, \end{cases}$$

onto the constraint set C_γ (21). Thus, we are led to the following scheme

$$\begin{aligned}\xi^{k+1} &= A\bar{\xi} - \frac{1}{\rho}\, (\mathrm{Id} - AA^* + A\Gamma A^*) \left(v^k - \rho\, e^k \right), \\ e^{k+1} &= \left[v^k + \rho\, \xi^{k+1} - \mathcal{P}_{C_\gamma}\left(v^k + \rho\, \xi^{k+1} \right) \right] / \rho, \\ v^{k+1} &= v^k + \rho\, (\xi^{k+1} - e^{k+1}).\end{aligned} \tag{34}$$

A recent study[77] highlighted the importance of utilizing a damping factor and choosing the penalty factor ρ adaptively. For this purpose, we consider the modified scheme

$$
\begin{aligned}
\xi^{k+1/2} &= A\bar{\xi} - \frac{1}{\rho^k}\ (\mathrm{Id} - AA^* + A\Gamma A^*)\left(v^k - \rho^k\ e^k\right),\\
\xi^{k+1} &= 2(1-\delta)\xi^{k+\frac{1}{2}} - (1-2\delta)e^k,\\
e^{k+1} &= \left[v^k + \rho^k\ \xi^{k+1} - \mathcal{P}_{C_\gamma}\left(v^k + \rho^k\ \xi^{k+1}\right)\right]/\rho^k,\\
v^{k+1} &= v^k + \rho^k\ (\xi^{k+1} - e^{k+1}).
\end{aligned}
\tag{35}
$$

with damping $\delta \in (0, 1)$ and adaptive penalty parameter ρ^k. In general, the overrelaxation $\delta = 1/4$ is recommended.[77,83,84] Simple choices for the parameter ρ^k are based on the Lorenz–Tran–Dinh scaling[85]

$$
\rho^k = \frac{\|v^k\|_{L^2}}{\|e^k\|_{L^2}}
$$

or the Barzilai–Borwein scaling[86]

$$
\rho^k = \frac{\langle v^k - v^{k-1}, e^k - e^{k-1}\rangle_{L^2}}{\|e^k - e^{k-1}\|^2_{L^2}}
$$

and an additional safeguard [77, sec. 2.5]. In our computational experiments, the latter two schemes outperform, both, constant penalty parameter ρ and residual balancing.[87]

Last but not least, let us stress that the operator Γ has an explicit form in Fourier space, see Willot et al. [88, eq. 18].

4 | COMPUTATIONAL EXPERIMENTS

4.1 | Setup

The algorithm (35) was integrated into an existing FFT-based computational homogenization code for thermal conductivity,[89] written in Python with Cython extensions (and OpenMP). In the context of small-strain inelasticity, the implementation of the ADMM (35) and the memory-efficient computation of the penalty factor is discussed in Schneider.[77] In the same paper, the convergence criterion

$$
\left\| e^k - \xi^{k+\frac{1}{2}} \right\|_{L^2} \leq \mathrm{tol}\ \left\| \langle v \rangle_Y \right\|, \tag{36}
$$

for prescribed tolerance tol, is identified as suitable. All computational experiments were run on a desktop computer with 32GB RAM and six 3.7GHz cores, and on a workstation with 512 GB RAM and two Intel Xeon(R) Gold 6146 processors (12×3.20 GHz), respectively. If not mentioned otherwise, we will use ADMM with damping factor $\delta = 0.25$ and the Barzilai–Borwein adaptive choice for the penalty factor. The default tolerance tol (36) was set to $\mathrm{tol} = 10^{-4}$.

4.2 | A single spherical inclusion

As a first example, we build upon previous numerical experiments [53, sec. 4.2.2] and compare the CCMF-discretization to previously investigated discretization schemes, namely, the rotated staggered grid[90-92] and the Moulinec–Suquet discretization.[93,94] We consider a 64^3 box containing a single spherical inclusion with a diameter of 32 voxels. The crack resistance of the inclusion is chosen as $\gamma_{\mathrm{sphere}} = 10\ \gamma_{\mathrm{matrix}}$. We prescribe a unit vector $\bar{\xi} = e_x$ in x-direction as the crack normal. We solved the problem up to a tolerance of 10^{-4} using ADMM and chose the penalty factor as lower bound $\rho = \min\{\gamma_{\mathrm{sphere}}, \gamma_{\mathrm{matrix}}\}$, which was the preferred choice for the primal-dual hybrid gradient method [53, sec. 3]. Solution fields on a central cross-section are shown in Figure 5.

The local flow fields v are shown in Figure 5A. The Moulinec–Suquets discretization shows significant artifacts, which is characteristic for Fourier spectral discretizations. The rotated staggered grid discretization, on the other hand, features checkerboard artifact, although at a lower degree. By contrast, the flow field corresponding to the CCMF-discretization is much smoother, similar to the explicit jump discretization in the context of thermal conductivity.[89,95] The differences

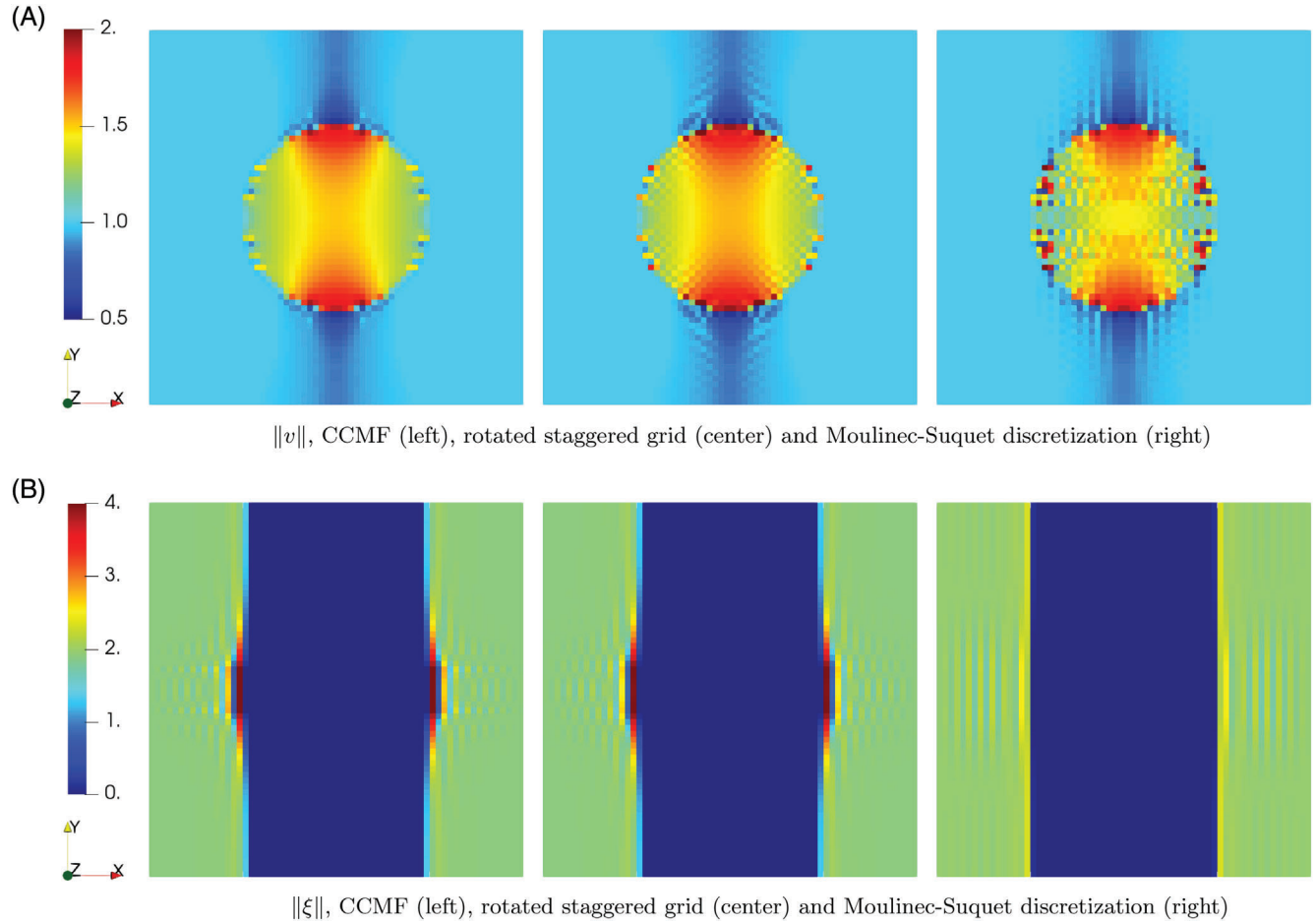

FIGURE 5 Flow v and normal ξ fields on a cross-section through a 64^3 single-sphere microstructure for $\bar{\xi} = e_x$, $\gamma_{\text{ball}} = 10\ \gamma_{\text{matrix}}$ and different discretizations

in the local crack-normal field ξ for the CCMF and the rotated staggered grid discretization are negligible and differ from the Moulinec–Suquet discretization in the local maximum values close to the central inclusion, see Figure 5B.

All discretization methods give rise to the same effective crack energy, that is, $\gamma_{\text{eff}} = \gamma_{\text{matrix}}$, as the crack bypasses the inclusion in a plane. This is independent of the material contrast, as long as the crack resistance of the matrix exceeds the crack resistance of the single sphere [53, sec. 4.2.2].

As the Moulinec–Suquet discretization shows the strongest artifacts, we focus on the remaining two discretization methods for the remaining investigations.

4.3 | A continuously fiber-reinforced composite

In this section, we wish to assess the performance of the ADMM solver introduced in Section 3. As a measure of verification, we choose a comparatively simple microstructure which enables us to employ a high-fidelity interior-point solver[96] for second-order cone programs. The latter produces high-precision solutions, but is limited in terms of problem size.

Accounting for this limitation, we consider a continuously fiber-reinforced composite with 50% filler content. The two-dimensional microstructure, containing 32 circular inclusions, was generated by the mechanical-contraction method[97] and discretized on a 128^2 voxel grid. The inclusions were furnished by a crack resistance of $\gamma_{\text{fiber}} = 10\ \gamma_{\text{matrix}}$. We investigate the effective crack energy in direction $\bar{\xi} = e_x$ and compare the CCMF discretization and the rotated staggered grid discretization, as well as different ADMM damping parameters δ, namely, $\delta = 0.25$ and $\delta = 0.5$. Furthermore, we investigate different selection strategies for the ADMM penalty-factor, the lower bound $\rho = \min\{\gamma_{\text{fiber}}, \gamma_{\text{matrix}}\}$, preferred in Schneider[53] and the Barzilai–Borwein scaling,[86] as well as the Lorenz–Tran Dinh scaling[85] and residual balancing.[87]

As announced earlier, we compare the effective crack energy to solutions obtained by the high-fidelity solver ECOS[96] applied to conic reformulations of the minimum-cut problem (24) for the CCMF scheme and the discretization on a rotated staggered grid. We assess the solver quality in terms of the relative error

$$\text{error} = \frac{|\gamma_{\text{eff}} - \gamma_{\text{eff}}^{\text{accurate}}|}{\gamma_{\text{eff}}^{\text{accurate}}} \tag{37}$$

in the effective crack energy, where $\gamma_{\text{eff}}^{\text{accurate}}$ is computed by the interior-point solver[96] with a residual of 10^{-10}.

Figure 6A shows the local flow field for, both the CCMF discretization and the rotated staggered grid discretization. For the rotated staggered grid, the flow field exhibits significant checkerboard artifacts in the inclusions as well as the matrix. The CCMF solution, on the other hand, is devoid of such artifacts. The corresponding crack paths are shown in Figure 6B. The cracks bypass the inclusions and look qualitatively similar for both discretizations. However, the rotated staggered grid discretization shows a wider crack path, whereas the CCMF crack path is sharper. This allows the CCMF crack path to avoid several inclusions in a straight line, whereas the rotated staggered grid crack path has to avoid them, resulting in a less straight crack path. This observation is also reflected in the resulting effective crack energy, that is, $\gamma_{\text{eff}} = 1.021\ \gamma_{\text{matrix}}$ for the rotated staggered grid and $\gamma_{\text{eff}} = 1.014\ \gamma_{\text{matrix}}$ for the CCMF discretization.

Figure 7A shows the residual of the solver versus the iteration count for the two strategies for selecting the penalty factor, two damping factors and the two discretizations under consideration. During the first 1000 iterations, all solvers behave similarly, with a slight advantage for the choice $\delta = 0.25$. After 2000 iterations, all solvers result in a residual below 10^{-3}. For the CCMF discretization, the ADMM solver with $\delta = 0.25$ and Barzilai–Borwein penalty-choice speeds up at 1600 iterations and reaches the required tolerance of 10^{-5} shortly thereafter. For $\delta = 0.5$ a similar acceleration occurs after slightly more than 8000 iterations. Selecting the lower bound for the penalty factor ρ does not reach the required tolerance within 10,000 iterations.

For the rotated staggered grid discretization, the Barzilai–Borwein penalty-factor outperforms the constant choice, as well. For this discretization, the difference between the two damping factor choices is much smaller than for CCMF.

The investigations are supplemented by Figure 7B, which records the associated relative error (37).

Indeed, the relation between the residual (36) and the error in the quantity of interest (37) is not directly apparent. We know that convergence of effective properties is implied by convergence of the fields. However, the quantitative relation between these may only be determined by comparison with a ground truth. For the CCMF discretizations, the relative error (37) correlates with the residual rather well, reaching an accuracy below 10^{-4} at convergence. By contrast, the solution for the rotated staggered grid leads to an error of only 0.5%, that is, hits a "stall."

In addition to the mentioned penalty-factor choices, we studied two further (less competitive) approaches, namely, residual balancing,[87] which is often recommended in the literature, as well as an the averaging approach suggested by Lorenz–Tran–Dinh,[85] which proved to be promising in small-strain micromechanics.[77] To increase readability, the residual and the error (37) were moved to Figure A1B of Appendix A.

With this validation at hand, we restrict to the CCMF discretization in combination with ADMM, damping factor $\delta = 0.25$ and the Barzilai–Borwein penalty-factor for the remainder of this work.

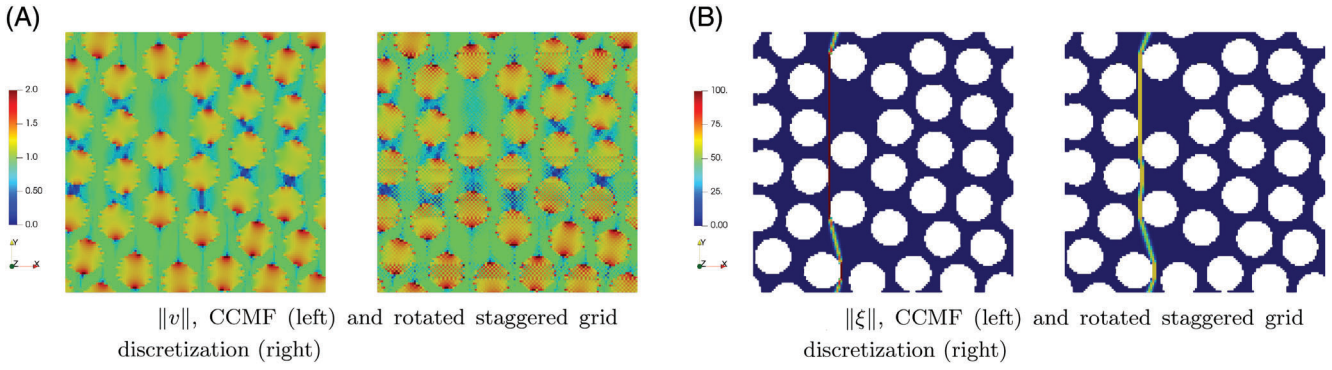

$\|v\|$, CCMF (left) and rotated staggered grid discretization (right)

$\|\xi\|$, CCMF (left) and rotated staggered grid discretization (right)

FIGURE 6 Cross-section through the solution fields v and ξ for a 128^2 microstructure, containing 32 circular inclusions for CCMF and rotated staggered grid discretization for $\overline{\xi} = e_x$ and $\gamma_{\text{fiber}} = 10\gamma_{\text{matrix}}$

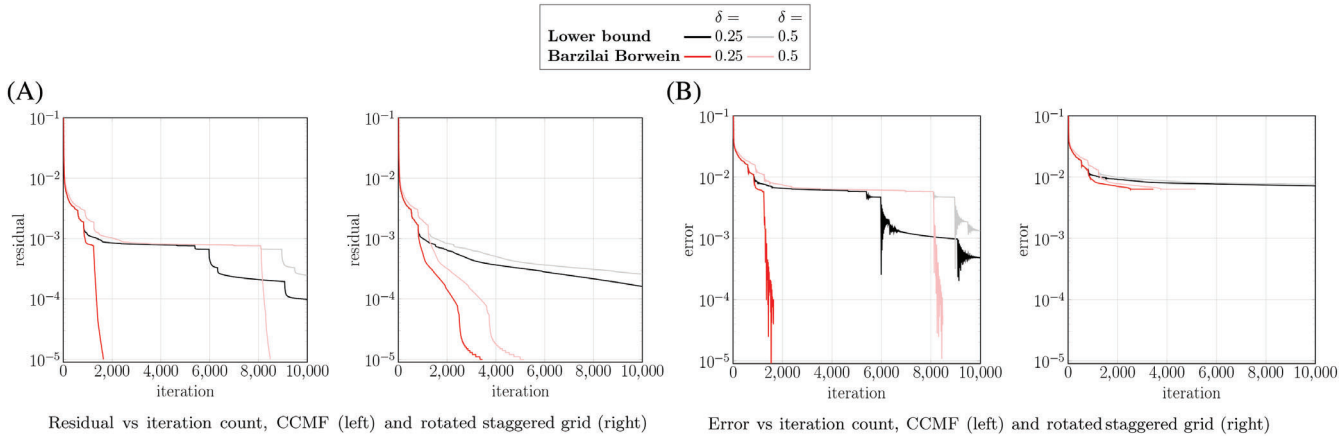

FIGURE 7 Residual and error measure (37) for CCMF and rotated staggered grid discretizations, comparing different solver parameters

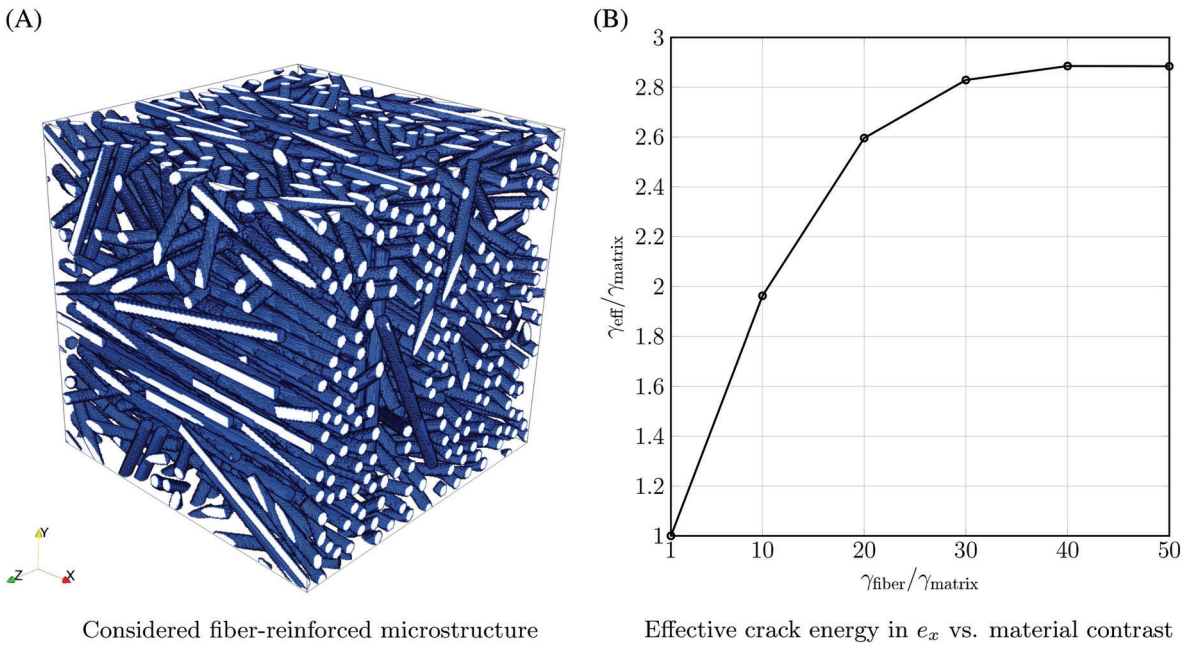

FIGURE 8 Microstructure and effective crack energy for the fiber-reinforced composite

4.4 | A fiber-reinforced composite

After the necessary verification steps, we turn our attention to problems with a higher degree of complexity. We consider a short-fiber reinforced composite with 18% filler content. The synthetic structure contains 376 fibers with an aspect ratio (length/diameter) of 20, and was generated by the SAM algorithm.[98] The prescribed fiber-orientation tensor of second order[99,100] was diag(0.75, 0.19, 0.06), that is, the fibers lie almost exclusively in the x-y-plane with a strong preference in x-direction. The fibers are discretized with eight voxels per diameter, resulting in a volume image with 256^3 voxels, see Figure 8A. Since the computations on such large structures are costly, we first investigate the influence of the tolerance entering the stopping criterion (36). For a configuration $\gamma_{\text{fiber}} = 50\ \gamma_{\text{matrix}}$, we computed the effective crack energy in direction $\bar{\xi} = e_x$. After 1000, 2500, 5000, 7500, and 10,000 iterations, we take a look at the corresponding residual and the computed effective crack energy, see Table 1. We observe that, after 1000 iterations we reach a residual of almost 10^{-3} with a relative deviation in effective crack energy about 2% compared with the prediction after 10,000 iterations. After 2500 iterations, the relative error is below 1% with a residual at about $6 \cdot 10^{-4}$. For more than 5000 iterations, the effective crack energy does not change in the third significant digit, whereas the residual decreases only slowly.

TABLE 1 Residual and computed effective crack energy with normal $\bar{\xi} = e_x$ depending on the number of ADMM iterations for a fiber-reinforced composite, see Figure 8A, with material parameters $\gamma_{\text{fiber}} = 50\ \gamma_{\text{matrix}}$

#Iterations	Residual	$\gamma_{\text{eff}}/\gamma_{\text{matrix}}$
1000	$1.7 \cdot 10^{-3}$	2.94
2500	$6.1 \cdot 10^{-4}$	2.89
5000	$1.9 \cdot 10^{-4}$	2.87
7500	$1.0 \cdot 10^{-4}$	2.87
10,000	$5.5 \cdot 10^{-5}$	2.87

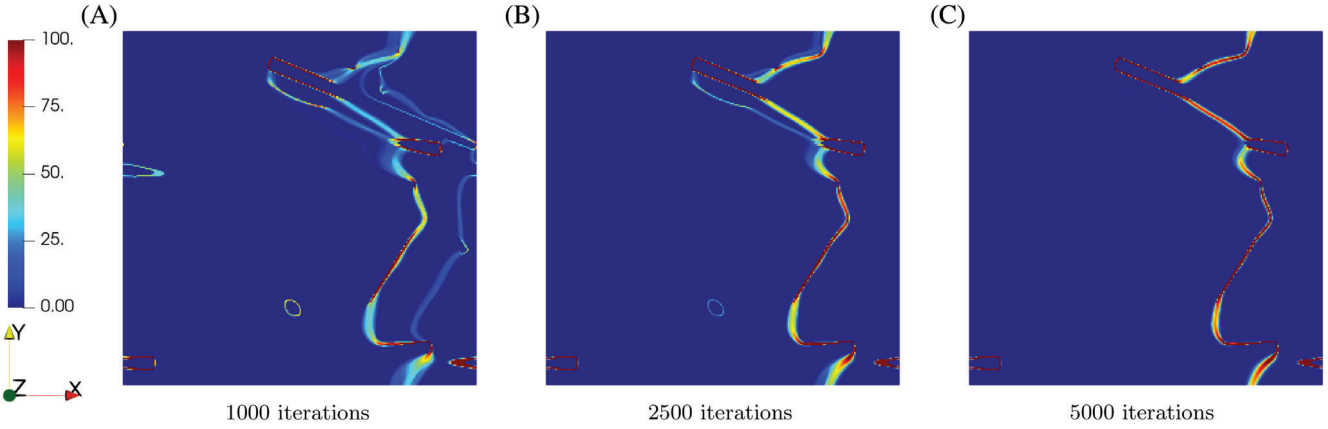

FIGURE 9 Cross-section through crack surface for $\gamma_{\text{fiber}} = 50\ \gamma_{\text{matrix}}$ at different ADMM iterations

To complement these numbers, we take a look at a cross-section through the computed crack surface at different iteration counts, see Figure 9. We observe an influence of the solver accuracy on the solution field ξ. Indeed, after 1000 iterations, several distinct crack paths are present in the vicinity of the solution. These different cracks, however, come with different "intensities," as well. This ambiguity is reduced after 2500 iterations. Only after 5000 iterations, the solver finds a unique crack surface.

Please note that, in general, we do not expect the minimum-cut problem (4) to have a unique solution. Rather, for the problem at hand, a unique crack is formed and, at low levels of the residual, additional cracks appear, compare also Schneider [53, sec. 4.1.2]. These vanish, however, at high accuracy.

To balance accuracy and ensuing computational costs, we fix the tolerance to $5 \cdot 10^{-4}$.

Next, we investigate the resulting crack surfaces and effective crack energies corresponding to different crack normals, see Figure 10. In e_x-direction, the effective crack energy is highest. This is caused by preferred fiber direction in this direction, forcing the crack surface to bypass the numerous inclusions. In e_y-direction, see Figure 10B, the crack surface looks roughly similar. However, the crack needs to avoid fewer fibers, resulting in a lower effective crack energy. In e_z-direction, the crack surface is almost straight, see Figure 10B, resulting in the lowest effective crack energy.

Last but not least, we investigate the influence of the material contrast on the computed effective crack energy in $\bar{\xi} = e_x$-direction, see Figure 8B. This contrast is responsible for the allowed crack-inclusion interaction-mechanisms. Indeed, for high contrast, the inclusions can only be avoided, that is, inclusion bypass is the only viable option. In general, the particles' anisotropy (encoded by the aspect ratio and the fiber orientation for the example at hand) and the filler content determine the threshold in contrast where only inclusion bypass is permitted. For the example at hand, Figure 8B reveals that this threshold is roughly at a material contrast of 40. In Table 2, the influence of the material contrast on the ADMM iteration count is listed. For a contrast of 10, the solver requires 404 iterations to reach the desired tolerance. Above a contrast of 20, the iteration count stabilizes at approximately 2700.

For lower contrast, it may be energetically more favorable to cross some of the inclusions. For decreasing material contrast, this inclusion-crossing mechanism occurs more frequently.

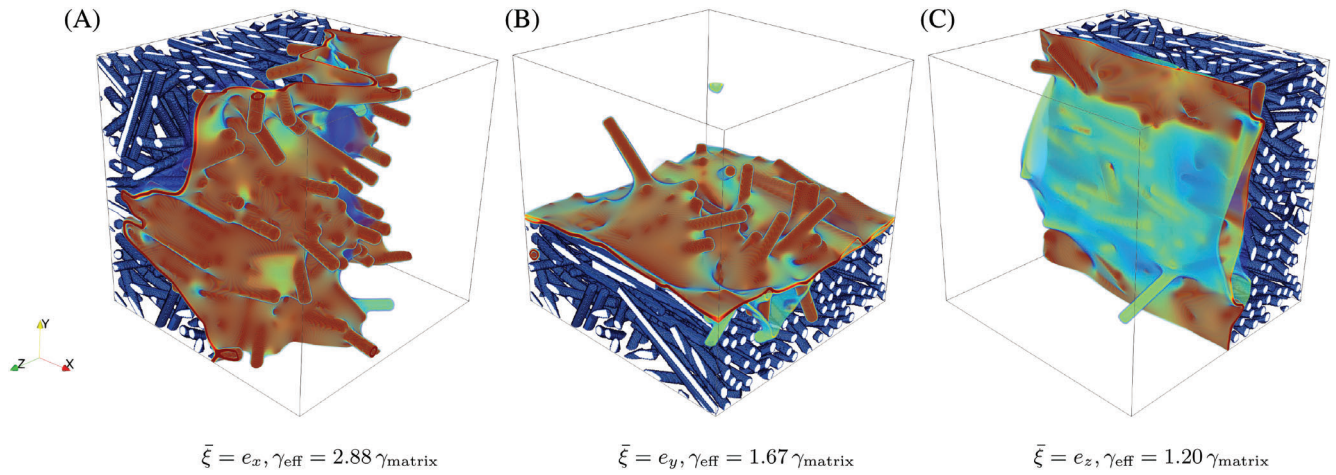

FIGURE 10 Crack surfaces for the Cartesian normals, material contrast $\gamma_{\text{fiber}}/\gamma_{\text{matrix}} = 50$ and the fiber-reinforced composite, see Figure 8A

TABLE 2 Number of ADMM iterations for varying material contrast $\gamma_{\text{fiber}}/\gamma_{\text{matrix}}$

$\gamma_{\text{fiber}}/\gamma_{\text{matrix}}$	#Iterations
10	404
20	2701
30	2633
40	2626
50	2717

4.5 | Microstructures with a monodisperse pore distribution

As our next example, we consider microstructures with monodisperse, spherical pores and varying degree of porosity. For a porosity between 5% and 50%, we generated microstructures with 200 spheres by the mechanical contraction method,[97] see Figure 11. All structures were discretized on a 256^3 voxel grid. The solid material has crack resistance γ, and the spherical pores are furnished with a vanishing crack resistance, resulting in an infinite material contrast. Please note that in the previous study [53, sec. 4.1.1], the pores were furnished with a nonvanishing (yet small) crack resistance to ensure robust convergence of the utilized solution scheme. Such a restriction appears unnecessary for the improved solution method presented in this article.

The effective crack energy in direction $\bar{\xi} = e_x$ and the required ADMM iterations are listed in Table 3. Following physical intuition, the effective crack energy decreases for increasing porosity. If the crack were straight, its crack energy would be proportional to the in-plane porosity of the crack plane. For a curved crack, there is a competition between "maximizing the porosity" and remaining as straight as possible, see Figure 11. The iteration count appears to be uncorrelated with the porosity. As a remark, we found the iteration count to be strongly dependent on the specific realization of the microstructure, in general. Thus, we expect that no such correlation may be inferred from a single sample, but would require a more elaborate study.

4.6 | Sand-binder composite

In our final example, we examine the microstructure of a sand-binder aggregate which is characteristic for inorganically bound sand cores used in casting applications. The synthetic structure was generated by a mechanical-contraction type method,[32,33] and is shown in Figure 1. The microstructure consists of three phases: The sand grains (58.6%),

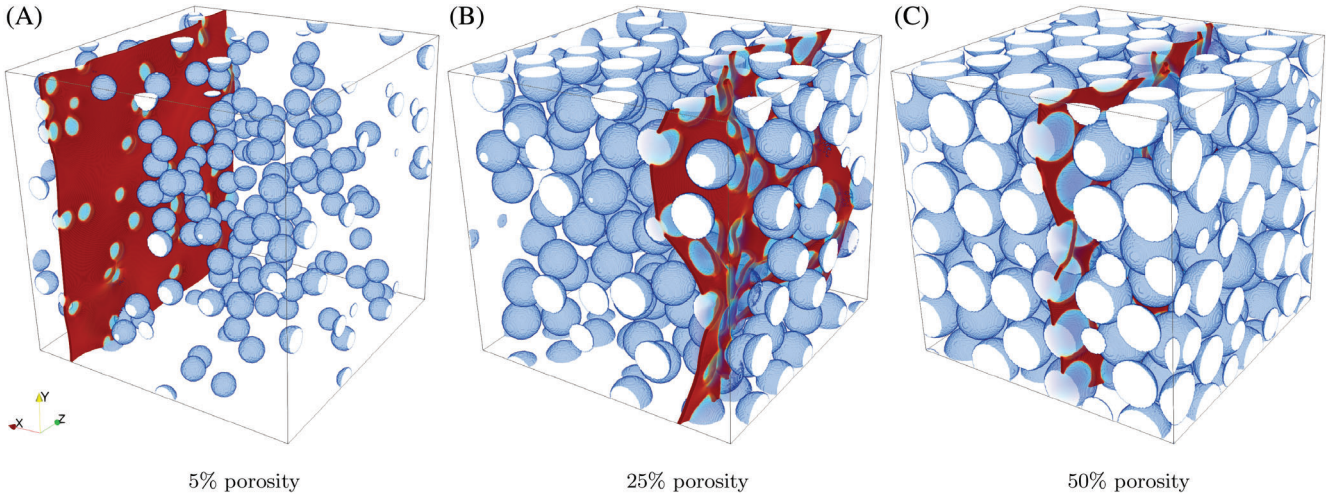

FIGURE 11 Crack surface through microstructures with varying porosity

TABLE 3 Influence of the porosity on the effective crack energy and solver performance for varying porosity

Porosity in %	$\gamma_{\text{eff}}/\gamma$	Iterations
5	0.871	4986
25	0.535	3300
40	0.412	3327
50	0.305	2358

TABLE 4 Material parameters, effective crack energies, as well as iteration count for the three cases under consideration

	γ_{matrix} in MPa·µm	γ_{grain} in MPa·µm	γ_{binder} in MPa·µm	γ_{eff} in MPa·µm	Iterations
#1	0	1	1	0.074	3204
#2	1	10	1	1.133	1711
#3	10	1	10	3.246	3971

connected by a binder phase (1.3%), and a third phase (40.1%). In the physical applications, the latter phase represents the pore space. We wish to utilize the microstructure to get insights for a number of physical scenarios, and we will refer to the third phase more generally as the "matrix" for reasons that will become clear shortly.

The crack resistances associated to the phases are denoted by γ_{grain}, γ_{binder}, and γ_{matrix}, respectively. To investigate the effective crack energy and possible crack surfaces through the microstructure, we consider three different parameter scenarios, where the single phases model different physical scenarios. The governing parameters and their resulting effective crack energy are listed in Table 4, together with the required iteration count. In parameter case #1, the crack resistance of the grains and the binder are equal, and the matrix material corresponds to a pore space. The resulting crack surface is shown in Figure 12A. We notice that the crack is fully contained in the binder phase. The effective crack energy is reduced to 7.5% of the crack resistance which grain and binder share. The second parameter case models the structure as a matrix material with tougher sand-grain inclusions. The binder phase is treated as additional matrix material. Figure 12B shows the crack surface avoiding the sand-grain shaped inclusions. The resulting effective crack energy of the composite is 1.133 γ_{matrix}. The third case deals with the same contrast, that is, the binder phase is once again treated as additional matrix. This time, however, the sand-grain shaped inclusions are weaker than the surrounding material. The effective

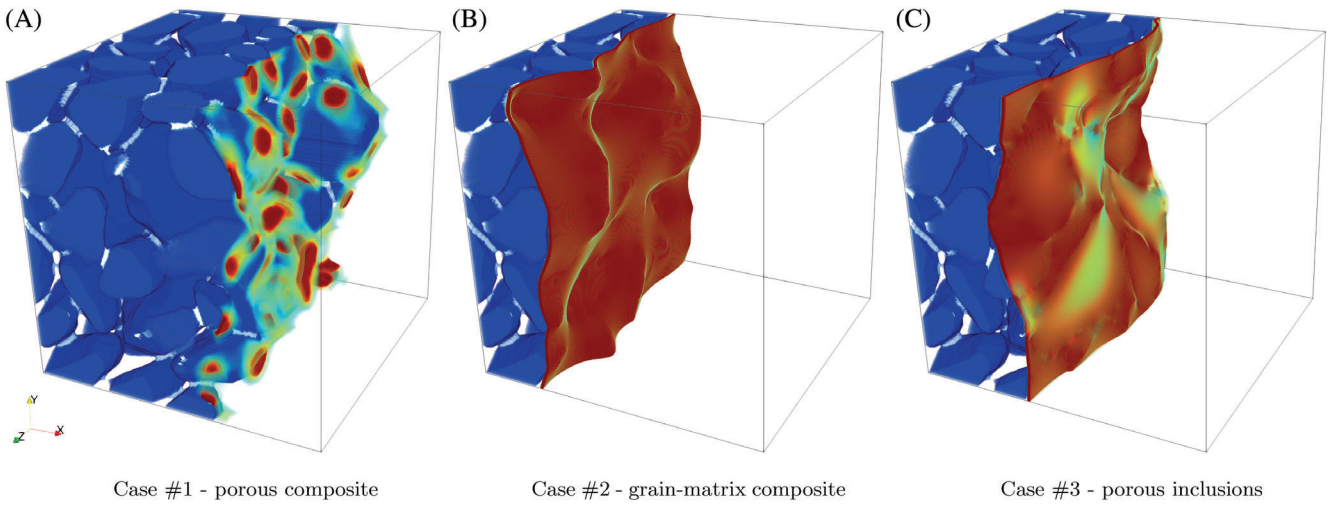

FIGURE 12 Crack surfaces through the bound sand-grain microstructure for three different combinations of crack resistances for matrix, inclusion, and binder

crack energy is 32% of the matrix crack resistance. Figure 12C shows the crack surface crossing several grains in order to avoid the matrix phase as much as possible.

5 | CONCLUSIONS

In this work, we presented a powerful FFT-based solution method for computing the effective crack energy of industrial-scale composite microstructures. Based on a homogenization result for the Francfort–Marigo model,[19] see Braides et al.[48] and following contributions,[54,59] a cell formula for computing the effective crack energy was investigated. This cell formula may be interpreted as a minimum cut/maximum flow problem,[64] which finds various applications, for instance in graph networks and image segmentation. Following Couprie et al.,[73] we considered the CCMF discretization on regular voxel data and integrated it into an FFT-based computational homogenization framework. In comparison with traditional spectral and finite-difference discretizations, we found the CCMF discretization to significantly reduce artifacts in the local fields.

For solving the discretized equations, we investigated the alternating direction method of multipliers (ADMM) with various adaptive strategies, and found a damping parameter $\delta = 0.25$ combined with the Barzilai–Borwein penalty-factor choice to be the most effective. We demonstrated the applicability of our approach to various large-scale problems, considering complex microstructures, as well as large or even infinite contrast in the local crack resistance. The presented framework was implemented into an existing homogenization code for thermal conductivity, and although we ran some computations on a workstation, all presented computations could be done on a conventional desktop computer.

Future work on this topic may focus on accounting for anisotropic crack resistance. This may be of interest in a two-step homogenization framework for braided or SMC composites,[101] and for brittle fracture in polycrystalline materials. Furthermore, accounting for weak interfaces may extend the applicability of the presented framework.

ACKNOWLEDGMENTS

Support by the German Research Foundation (DFG) within the International Research Training Group "Integrated engineering of continuous-discontinuous long fiber reinforced polymer structures" (GRK 2078) and in terms of the project SCHN 1595/2-1 is gratefully acknowledged. The authors thank S. Gajek (KIT), M. Lebihain (EPFL Lausanne), and D. Kondo (Sorbonne) for fruitful discussions.

DATA AVAILABILITY STATEMENT

The data that support the findings of this study are available from the corresponding author upon reasonable request.

ORCID

Matti Schneider https://orcid.org/0000-0001-7017-3618

REFERENCES

1. Gross D, Seelig T. *Fracture Mechanics*. Mechanical Engineering Series. 3rd ed. New York, NY: Springer; 2017.
2. Griffith AA. The phenomena of rupture and flow in solids. *Philos Trans R Soc Lond A*. 1921;221:163-198.
3. Irwin GR. Analysis of stresses and strains near the end of a crack transversing a plate. *J Appl Mech*. 1957;24:361-364.
4. Irwin GR. Crack-extension force for a part-through crack in a plate. *J Appl Mech*. 1962;29:2281-2291.
5. Cherepanov GP. The propagation of cracks in a continuous medium. *J Appl Math Mech*. 1967;31(3):503-512.
6. Rice JR. A path independent integral and the approximate analysis of strain concentration by notches and cracks. *J Appl Mech*. 1968;35:379-386.
7. Gol'dstein RV, Salganik RL. Brittle fracture of solids with arbitrary cracks. *Int J Fract*. 1974;10:507-523.
8. Hussain MA, Pu S, Underwood J. Strain Energy Release Rate for a Crack Under Combined Mode I and Mode II, In: Irwin G, ed. *Fracture Analysis: Proceedings of the 1973 National Symposium on Fracture Mechanics, Part II*. West Conshohocken, PA: ASTM International; 1974:2-28.
9. Dugdale DS. Yielding of steel sheets containing slits. *J Mech Phys Solids*. 1960;8:100-104.
10. Barenblatt GI. The mathematical theory of equilibrium cracks in brittle fracture. *Adv Appl Mech*. 1962;7:55-129.
11. Rice JR, Tracey DM. Computational fracture mechanics. In: Fenves SJ, et al., eds. *Numerical and Computer Methods in Structural Mechanics*. Cambridge, MA: Academic Press; 1973:585-623.
12. Moës N, Dolbow J, Belytschko T. A finite element method for crack growth without remeshing. *Int J Numer Methods Eng*. 1999;46(1):131-150.
13. Fries T-P, Belytschko T. The extended/generalized finite element method: An overview of the method and its applications. *Int J Numer Methods Eng*. 2010;84(3):253-304.
14. Sih GC, Paris PC, Irwin GR. On cracks in rectilinearly anisotropic bodies. *Int J Fract Mech*. 1965;1:189-203.
15. Wu EM. Application of fracture mechanics to anisotropic plates. *J Appl Mech*. 1967;34(4):967-974.
16. Saouma VE, Ayari ML, Leavell DA. Mixed mode crack propagation in homogeneous anisotropic solids. *Eng Fract Mech*. 1987;27(2):171-184.
17. Williams JG. Chapter 1 - fracture mechanics of anisotropic materials. In: Friedrich K, ed. *Application of Fracture Mechanics to Composite Materials. Composite Materials Series*. Vol 6. Amsterdam, Netherlands: Elsevier; 1989:3-38. https://www.sciencedirect.com/science/article/pii/B978044487286950005X.
18. Laubie HH. *Linear Elastic Fracture Mechanics in Anisotropic Solids: Application to Fluid-Driven Crack Propagation* [PhD thesis]. Massachusetts Institute of Technology; 2013.
19. Francfort GA, Marigo J-J. Revisiting brittle fracture as an energy minimization problem. *J Mech Phys Solids*. 1998;46(8):1319-1342.
20. Chambolle A, Crismale V. Existence of strong solutions to the Dirichlet problem for the Griffith energy. *Calc Var PDE*. 2019;58(4):136.
21. Bourdin B. Numerical implementation of the variational formulation for quasi-static brittle fracture. *Interf Free Bound*. 2007;9:411-430.
22. Dimitrijevic BJ, Hackl K. A method for gradient enhancement of continuum damage models. *Tech Mech*. 2008;28:43-52.
23. Bažant ZP. Why continuum damage is nonlocal: micromechanics argument. *J Eng Mech*. 1991;117:1070-1087.
24. Kuhn C, Müller R. A continuum phase field model for fracture. *Eng Fract Mech*. 2010;77(18):3625-3634.
25. Miehe C, Hofacker M, Welschinger F. A phase field model for rate-independent crack propagation: robust algorithmic implementation based on operator splits. *Comput Methods Appl Mech Eng*. 2010;199:2765-2778. https://www.sciencedirect.com/science/article/pii/S0045782510001283.
26. Ambati M, Gerasimov T, De Lorenzis L. A review on phase-field models of brittle fracture and a new fast hybrid formulation. *Comput Mech*. 2015;55:383-405.
27. Prajapati N, Herrmann C, Späth M, Schneider D, Selzer M, Nestler B. Brittle anisotropic fracture propagation in quartz sandstone: insights from phase-field simulations. *Comput Geosci*. 2020;24:1361-1376.
28. Teichmeister S, Kienle D, Aldakheel F, Keip M-A. Phase field modeling of fracture in anisotropic brittle solids. *Int J Non-Linear Mech*. 2017;97:1-21.
29. Schreiber C, Ettrich T, Kuhn C, Müller R. A phase field modeling approach of crack growth in materials with anisotropic fracture toughness. In: Garth C, Aurich JC Linke B, et al., eds. *2nd International Conference of the DFG International Research Training Group 2057 - Physical Modeling for Virtual Manufacturing (iPMVM 2020). Open Access Series in Informatics (OASIcs)*. Vol 89. Dagstuhl, Germany: Schloss Dagstuhl – Leibniz-Zentrum für Informatik; 2021:9:1-9:17.
30. Matouš K, Geers MGD, Kouznetsova VG, Gillman A. A review of predictive nonlinear theories for multiscale modeling of heterogeneous materials. *J Comput Phys*. 2017;330:192-220.
31. Gitman IM, Askes H, Sluys L. Representative volume: existence and size determination. *Eng Fract Mech*. 2007;74:2518-2534.
32. Schneider M, Hofmann T, Andrä H. Modelling the microstructure and computing effective elastic properties of sand core materials. *Int J Solids Struct*. 2018;143:1-17.
33. Ettemeyer F, Lechner P, Hofmann T. Digital sand core physics: predicting physical properties of sand cores by simulations on digital microstructures. *Int J Solids Struct*. 2020;188-189:155-168.

34. Berthier E, Ponson L, Dascalu C. Quasi-brittle fracture of heterogeneous materials: a nonlocal damage model. *Proc Mater Sci*. 2014;3:1878-1883.
35. Boeff M, Gutknecht F, Engels PS, Ma A, Hartmaier A. Formulation of nonlocal damage models based on spectral methods for application to complex microstructures. *Eng Fract Mech*. 2015;147:373-387.
36. Nguyen T-T, Yvonnet J, Zhu Q-Z, Bornet M, Chateau C. A phase-field method for computational modeling of interfacial damage interacting with crack propagation in realistic microstructures obtained by microtomography. *Comput Methods Appl Mech Eng*. 2016;312:567-595.
37. Chen Y, Vasiukov D, Gélébart L, Park CH. A FFT solver for variational phase-field modeling of brittle fracture. *Comput Methods Appl Mech Eng*. 2019;349:167-190.
38. Ernesti F, Schneider M, Böhlke T. Fast implicit solvers for phase field fracture problems on heterogeneous microstructures. *Comput Methods Appl Mech Eng*. 2020;363:112793.
39. Bower AF, Ortiz M. A three-dimensional analysis of crack trapping and bridging by tough particles. *J Mech Phys Solids*. 1991;39:815-858.
40. Roux S, Vandembroucq D, Hild F. Effective toughness of heterogeneous brittle materials. *Eur J Mech A/Solids*. 2003;22:743-749.
41. Démery V, Rosso A, Ponson L. From microstructural features to effective toughness in disordered brittle solids. *EPL (Europhys Lett)*. 2014;105:34003.
42. Lebihain M. *Large-Scale Crack Propagation in Heterogeneous Materials: An Insight into the Homogenization of Brittle Fracture Properties* [PhD dissertation]. Sorbonne Université; 2019.
43. Lebihain M, Ponson L, Kondo D, Leblond J-B. Effective toughness of disordered brittle solids: a homogenization framework. *J Mech Phys Solids*. 2021;153:104463.
44. Rice J. First-order variation in elastic fields due to variation in location of a planar crack front. *J Appl Mech*. 1985;52:571-579.
45. Hossain MZ, Hsueh C-J, Bourdin B, Bhattacharya K. Effective toughness of heterogeneous media. *J Mech Phys Solids*. 2014;71:15-32.
46. Kuhn C, Müller R. A discussion of fracture mechanisms in heterogeneous materials by means of configurational forces in a phase field fracture model. *Comput Methods Appl Mech Eng*. 2016;312:95-116.
47. Brach S, Hossain MZ, Bourdin B, Bhattacharya K. Anisotropy of the effective toughness of layered media. *J Mech Phys Solids*. 2019;131:96-111.
48. Braides A, Defranceschi A, Vitali E. Homogenization of free discontinuity problems. *Arch Ration Mech Anal*. 1996;135:297-356.
49. Milton GW. *The Theory of Composites*. Cambridge, MA: Cambridge University Press; 2002.
50. Kanit T, Forest S, Galliet I, Mounoury V, Jeulin D. Determination of the size of the representative volume element for random composites: statistical and numerical approach. *J Mech Phys Solids*. 2003;40(13–14):3647-3679.
51. Owhadi H. Approximation of the effective conductivity of ergodic media by periodization. *Probab Theory Relat Fields*. 2003;125:225-258.
52. Bourgeat A, Piatnitski A. Approximations of effective coefficients in stochastic homogenization. *Annales de l'Intitut H Poincaré*. 2004;40:153-165.
53. Schneider M. An FFT-based method for computing weighted minimal surfaces in microstructures with applications to the computational homogenization of brittle fracture. *Int J Numer Methods Eng*. 2020;121(7):1367-1387.
54. Cagnetti F, Dal Maso G, Scardia L, Zeppieri CI. Stochastic homogenization of free-discontinuity problems. *Arch Ration Mech Anal*. 2019;233:935-974.
55. Hill R. Elastic properties of reinforced solids: some theoretical principles. *J Mech Phys Solids*. 1963;11(5):357-372.
56. Drugan W, Willis JR. A micromechanics-based nonlocal constitutive equations and estimates of representative volume element size for elastic composites. *J Mech Phys Solids*. 1996;44:497-524.
57. Barchiesi M, Lazzaroni G, Zeppieri CI. A bridging mechanism in the homogenisation of brittle composites with soft inclusions. *SIAM J Math Anal*. 2016;48(2):1178-1209.
58. Pellet X, Scardia L, Zeppieri CI. Homogenisation of high-contrast Mumford-Shah energies. *SIAM J Math Anal*. 2019;51(3):1035-1079.
59. Friedrich M. A compactness result in $GSBV^p$ and applications to Γ-convergence for free discontinuity problems. *Calc Var*. 2019;58:86.
60. Bach A, Marziani R, Zeppieri CI. Γ convergence and stochastic homogenization of singularly-perturbed elliptic functionals. *Cal Var Geometr Measure Theory Pisa*. 2021;(5031):1-48.
61. Jeulin D. On image analysis and micromechanics. *Revue de Physique Appliquée*. 1988;23(4):549-556.
62. Sethian JA. *Level Set Methods and Fast Marching Methods*. Cambridge, MA: Cambridge University Press; 1999.
63. Osher SJ, Fedkiw R. *Level Set Methods and Dynamic Implicit Surfaces*. New York, NY: Springer; 2002.
64. Strang G. Maximal flow through a domain. *Math Program*. 1983;26:123-143.
65. Esser E, Zhang X, Chan TF. A general framework for a class of first order primal-dual algorithms for convex optimization in imaging science. *SIAM J Imaging Sci*. 2010;3(4):1015-1046.
66. Pock T, Cremers D, Bischof H, Chambolle A. An algorithm for minimizing the Mumford-Shah functional. Paper presented at: Proceedings of the ICCV; 2009; LNCS, Springer, New York, NY.
67. Ford LR, Fulkerson DR. Maximal flow through a network. *Can J Math*. 1956;8:399-404.
68. Elias P, Feinstein A, Shannon CE. A note on the maximum flow through a network. *IRE Trans Inf Theory*. 1956;2(4):117-119.
69. Dinic EA. Algorithm for solution of a problem of maximum flow in a network with power estimation. *Soviet Math Doklady*. 1970;11:1277-1280.
70. Edmonds J, Karp RM. Theoretical improvements in algorithmic efficiency for network flow problems. *J ACM*. 1972;19(2):248-264.
71. Goldberg AV, Rao S. Beyond the flow decomposition barrier. *J ACM*. 1998;45(5):783-797.
72. Kolmogorov V, Zabih R. What energy functions can be minimized via graph cuts? *IEEE Trans Pattern Anal Mach Intell*. 2004;26:147-159.

73. Couprie C, Grady L, Talbot H, Najman L. Combinatorial continuous maximum flow. *SIAM J Imaging Sci*. 2011;4(3):905-930.
74. Boyd S, Vandenberghe L. *Convex Optimization*. Cambridge, MA: Cambridge University Press; 2004.
75. Michel JC, Moulinec H, Suquet P. A computational method based on augmented lagrangians and fast fourier transforms for composites with high contrast. *Comput Model Eng Sci*. 2000;1(2):79-88.
76. Michel JC, Moulinec H, Suquet P. A computational scheme for linear and non-linear composites with arbitrary phase contrast. *Int J Numer Methods Eng*. 2001;52:139-160.
77. Schneider M. Non-stationary polarization methods in FFT-based computational micromechanics. *Int J Numer Methods Eng*. 2021;1-30.
78. Willot F. The effective conductivity of strongly nonlinear media: the dilute limit. *Int J Solids Struct*. 2020;184:287-295.
79. Chambolle A, Pock T. An introduction to continuous optimization for imaging. *Acta Numer*. 2016;25:161-319.
80. Nozawa R. Examples of max-flow and min-cut problems with duality gaps in continuous networks. *Math Program*. 1994;63:213-234.
81. Glowinski R, Marrocco A. Sur l'approximation, par éléments finis d'ordre un, et la résolution, par pénalisation-dualité d'une classe de problèmes de Dirichlet non linéares. *ESAIM Math Modell Numer Anal - Modélisation Mathématique et Analyse Numérique*. 1975;9:41-76. http://www.numdam.org/item/M2AN_1975__9_2_41_0/.
82. Gabay D, Mercier B. A dual algorithm for the solution of nonlinear variational problems via finite element approximations. *Comput Math Appl*. 1976;2(1):17-40.
83. Monchiet V, Bonnet G. A polarization-based FFT iterative scheme for computing the effective properties of elastic composites with arbitrary contrast. *Int J Numer Methods Eng*. 2012;89:1419-1436.
84. Moulinec H, Silva F. Comparison of three accelerated FFT-based schemes for computing the mechanical response of composite materials. *Int J Numer Methods Eng*. 2014;97(13):960-985.
85. Lorenz DA, Tran-Dinh Q. Non-stationary Douglas-Rachford and alternating direction method of multipliers: adaptive step-sizes and convergence. *Comput Optim Appl*. 2019;74:67-92.
86. Xu Z, Figueiredo MAT, Goldstein T. Adaptive ADMM with spectral penalty parameter selection. In: Singh A, Zhu J, eds. Proceedings of the 20th International Conference on Artificial Intelligence and Statistics *Proceedings of Machine Learning Research*. Vol 54. Fort Lauderdale, FL: PMLR; 2017:718-727. http://proceedings.mlr.press/v54/xu17a.
87. He BS, Yang H, Wang SL. Alternating direction method with self-adaptive penalty parameters for monotone variational inequalities. *J Optim Theory Appl*. 2000;106(2):337-356.
88. Willot F, Abdallah B, Pellegrini Y-P. Fourier-based schemes with modified Green operator for computing the electrical response of heterogeneous media with accurate local fields. *Int J Numer Methods Eng*. 2014;98(7):518-533.
89. Dorn C, Schneider M. Lippmann-Schwinger solvers for the explicit jump discretization for thermal computational homogenization problems. *Int J Numer Methods Eng*. 2019;118(11):631-653.
90. Saenger EH, Gold N, Shapiro SA. Modeling the propagation of elastic waves using a modified finite-difference grid. *Wave Motion*. 2000;31(1):77-92.
91. Saenger EH, Bohlen T. Finite-difference modeling of viscoelastic and anisotropic wave propagation using the rotated staggered grid. *Geophysics*. 2004;69(2):583-591.
92. Willot F. Fourier-based schemes for computing the mechanical response of composites with accurate local fields. *Comptes Rendus Mécanique*. 2015;343:232-245.
93. Moulinec H, Suquet P. A fast numerical method for computing the linear and nonlinear mechanical properties of composites. *Comptes Rendus de l'Académie des Sciences Série II*. 1994;318(11):1417-1423.
94. Moulinec H, Suquet P. A numerical method for computing the overall response of nonlinear composites with complex microstructure. *Comput Methods Appl Mech Eng*. 1998;157:69-94.
95. Wiegmann A, Zemitis A. EJ-HEAT: a fast explicit jump harmonic averaging solver for the effective heat conductivity of composite materials. *Berichte des Fraunhofer ITWM*. 2006;94:1-21.
96. Domahidi A, Chu E, Boyd S. ECOS: an SOCP solver for embedded systems. Paper presented at: Proceedings of the 2013 European Control Conference (ECC); 2013:3071-3076; Zurich.
97. Williams S, Philipse A. Random packings of spheres and spherocylinders simulated by mechanical contraction. *Phys Rev E*. 2003;67:1-9.
98. Schneider M. The sequential addition and migration method to generate representative volume elements for the homogenization of short fiber reinforced plastics. *Comput Mech*. 2017;59:247-263.
99. Kanatani K. Distribution of directional data and fabric tensors. *Int J Eng Sci*. 1984;22:149-164.
100. Advani SG, Tucker CL. The use of tensors to describe and predict fiber orientation in short fiber composites. *J Rheol*. 1987;31:751-784.
101. Görthofer J, Schneider M, Ospald F, Hrymak A, Böhlke T. Computational homogenization of sheet molding compound composites based on high fidelity representative volume elements. *Comput Mater Sci*. 2020;174:109456.

How to cite this article: Ernesti F, Schneider M. A fast Fourier transform based method for computing the effective crack energy of a heterogeneous material on a combinatorially consistent grid. *Int J Numer Methods Eng*. 2021;1–25. https://doi.org/10.1002/nme.6792

APPENDIX A. PERFORMANCE OF ADDITIONAL PENALTY FACTOR CHOICES

In addition to the lower bound and the Barzilai–Borwein strategy for choosing the penalty factor ρ in combination with different damping parameters δ, see Section 4.3, we investigated two additional choices which are popular in the literature. More precisely, we consider residual balancing[87] and the averaging strategy proposed by Lorenz–Tran–Dinh,[85] which perform admirably for linear elastic and inelastic homogenization problems.[77] The resulting residual and error plots are shown in Figure A1. For the CCMF-discretization and the damping parameter $\delta = 0.5$, the residual balancing strategy led to an unstable behavior. The choice $\delta = 0.25$ resolves this instability. However, this approach does not lead to a high accurate solution. The averaging strategy by Lorenz–Tran–Dinh[85] shows more promising results, reaching a tolerance of 10^{-4} in fewer than 2000 iterations and $\delta = 0.25$. However, this parameter choice turns out to be inferior to the Barzilai–Borwein approach. The relative error (37), shown in Figure A1B correlates with the residual in a similar way as for the choices considered in Section 4.3. For the rotated staggered grid discretization, the Lorenz–Tran–Dinh scaling with $\delta = 0.25$ shows the best performance. However, only low accuracy in terms of the relative error (37) may be reached.

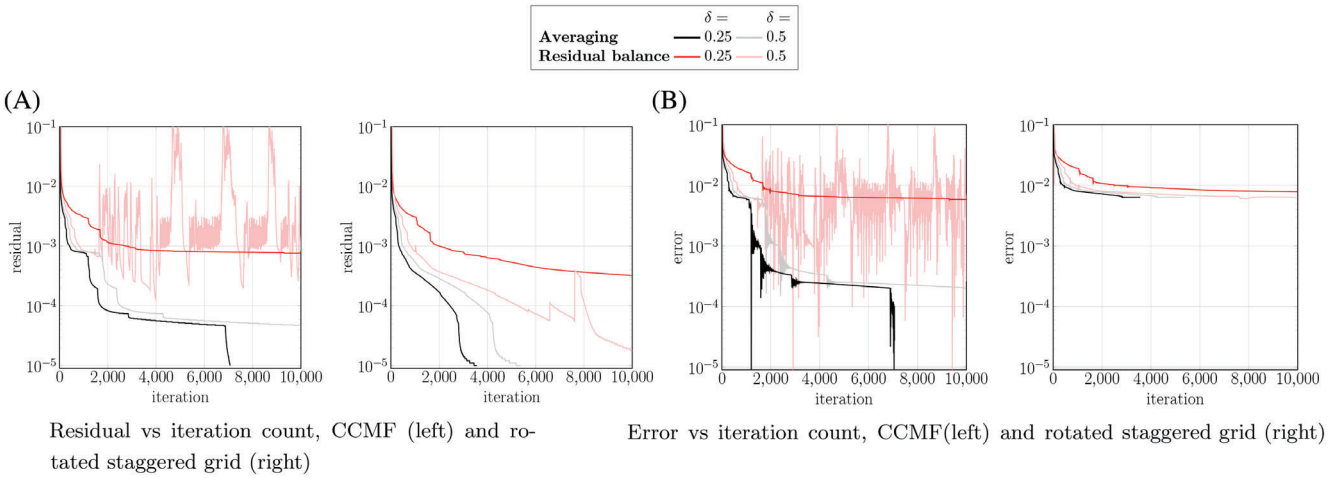

FIGURE A1 Residual and error measure for CCMF and rotated staggered grid discretizations, comparing different solver parameters